

1 Understanding the spatiotemporal variability of tropical orographic rainfall

2 using convective plume buoyancy

Quentin Nicolas^a and William R. Boos^{a,b}

^a Department of Earth and Planetary Science, University of California, Berkeley, California

⁵ ^b Climate and Ecosystem Sciences Division, Lawrence Berkeley National Laboratory, Berkeley,
⁶ California

⁷ Corresponding author: Quentin Nicolas, qnicolas@berkeley.edu

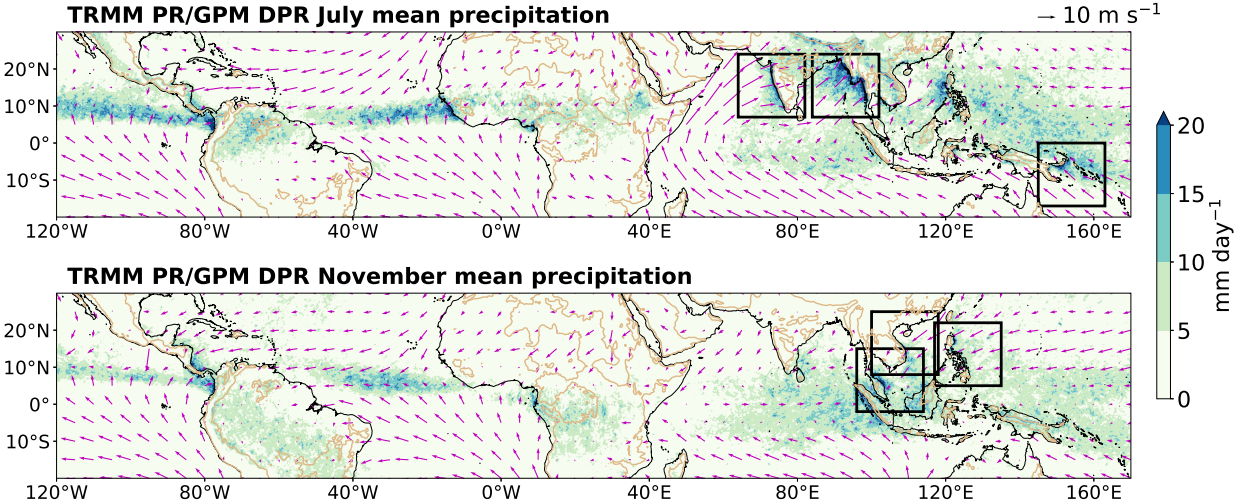
8 ABSTRACT: Mechanical forcing by orography affects precipitating convection across many trop-
9 ical regions, but controls on the intensity and horizontal extent of the orographic precipitation
10 peak and rain shadow remain poorly understood. A recent theory explains this control of precip-
11 itation as arising from modulation of lower-tropospheric temperature and moisture by orographic
12 mechanical forcing, setting the distribution of convective rainfall by controlling parcel buoyancy.
13 Using satellite and reanalysis data, we evaluate this theory by investigating spatiotemporal precip-
14 itation variations in six mountainous tropical regions spanning South and Southeast Asia, and the
15 Maritime Continent. We show that a strong relationship holds in these regions between daily pre-
16 cipitation and a measure of convective plume buoyancy. This measure depends on boundary layer
17 thermodynamic properties and lower-free-tropospheric moisture and temperature. Consistent with
18 the theory, temporal variations in lower-free-tropospheric temperature are primarily modulated by
19 orographic mechanical lifting through changes in cross-slope wind speed. However, winds di-
20 rected along background horizontal moisture gradients also influence lower-tropospheric moisture
21 variations in some regions. The buoyancy measure is also shown to explain many aspects of the
22 spatial patterns of precipitation. Finally, we present a linear model with two horizontal dimen-
23 sions that combines mountain wave dynamics with a linearized closure exploiting the relationship
24 between precipitation and plume buoyancy. In some regions, this model skillfully captures the
25 spatial structure and intensity of rainfall; it underestimates rainfall in regions where time-mean
26 ascent in large-scale convergence zones shapes lower-tropospheric humidity. Overall, these results
27 provide new understanding of fundamental processes controlling subseasonal and spatial variations
28 in tropical orographic precipitation.

29 **1. Introduction**

30 Mountains shape rainfall distributions in many of Earth's tropical land regions, modifying the
31 thermodynamic environment by interacting with large-scale winds or altering surface fluxes. With
32 over 2.5 billion people living in mountainous areas and another 2 billion in lowland areas depending
33 on mountain water resources (Viviroli et al. 2020), orographic precipitation is currently the main
34 water source for over 55% of the world's population, with a majority of that fraction located in
35 the tropics. It is also the main source of energy for hydropower, which is the primary resource for
36 renewable electricity generation globally, and a potential cause of dam failures when occurring in
37 excess (Li et al. 2022).

38 Orographic rainfall features large spatial gradients, with vastly different hydrological conditions
39 upwind and downwind of ridges. In the tropics, strong precipitation gradients are widely observed
40 along local orography in South and Southeast Asia, the Maritime Continent, and the northern and
41 central Andes (Fig. 1). The spatial structure of orographic precipitation has been studied in various
42 regions across the tropics, with examples including the Ethiopian Highlands (Van den Hende et al.
43 2021), the Andes (Espinoza et al. 2015), the Western Ghats (e.g., Tawde and Singh 2015) and
44 the Arakan Yoma range of Myanmar (e.g., Shige et al. 2017). The qualitative picture behind this
45 spatial organization is widely known: mountains force low-level ascent on their upwind flanks,
46 which, with sufficient moisture, drives condensation and precipitation (Smith 1979; Roe 2005).
47 The subsiding downstream flow, conversely, is warm and dry. Yet this paradigm, which assumes
48 layer-wise ascent and saturation, is unlikely to be quantitatively accurate in tropical regions where
49 most rainfall stems from convection (Kirshbaum et al. 2018) and where even simple questions, such
50 as what sets the upstream extent of orographic rainfall enhancement, have been debated (Smith
51 and Lin 1983; Grossman and Durran 1984). This study aims to address this issue and related open
52 questions (such as controls on rain shadow extent and the amplitude of rainfall maxima), taking
53 several tropical regions as examples.

57 In midlatitudes, column-integrated water vapor transport (IVT) has been proposed as a dom-
58 inant control on orographic precipitation (Sawyer 1956; Smith 2019). Indeed, in the idealized
59 picture of forced ascent over an orographic barrier, IVT modulates the condensation rate over the
60 upwind slopes. Additionally, stronger IVT typically results in a smaller nondimensional mountain
61 height (through both stronger winds and a smaller effective static stability), causing flow to ascend



54 FIG. 1. TRMM PR and GPM DPR near-surface precipitation, 500 m surface height level (thin brown contours),
55 and ERA5 wind vectors 100 m above the surface averaged over July (top) and November (bottom) from 2001 to
56 2020. See section 2 for details on the data products.

62 rather than detour around mountains (Smith 1989; Kirshbaum and Smith 2008). Other controls
63 on midlatitude orographic precipitation include mountain slope and temperature-mediated micro-
64 physical effects (Kirshbaum and Smith 2008). The spatial organization of orographic precipitation
65 in convectively stable flows has been understood through the influence of topography on vertical
66 velocities in saturated flows, with a contribution from the downwind advection of hydrometeors
67 (Smith and Barstad 2004, hereafter SB04).

68 Orographic precipitation generally occurs in association with various types of disturbances, from
69 frontal systems in midlatitude winter to deep convective systems in parts of the tropics (Houze
70 2012). We illustrate these in Fig. 2, which shows instantaneous radar reflectivity from the
71 Global Precipitation Measurement (GPM) Ku-band radar (Seto et al. 2021) for two cases. The
72 first illustrates a winter frontal system over coastal mountains of British Columbia and features
73 a horizontally wide, vertically shallow signal with a sloping bright band (visible between 300
74 and 550 km at 2 km altitude in the vertical cross-section), characteristic of frontal ascent. In
75 contrast, the Western Ghats case, during the summer monsoon, features smaller scale, stronger
76 echoes reaching deeper heights (up to 10 km; note that summertime convection in and upstream
77 of the Western Ghats is shallower than in the rest of the tropics, see Kumar and Bhat 2017).

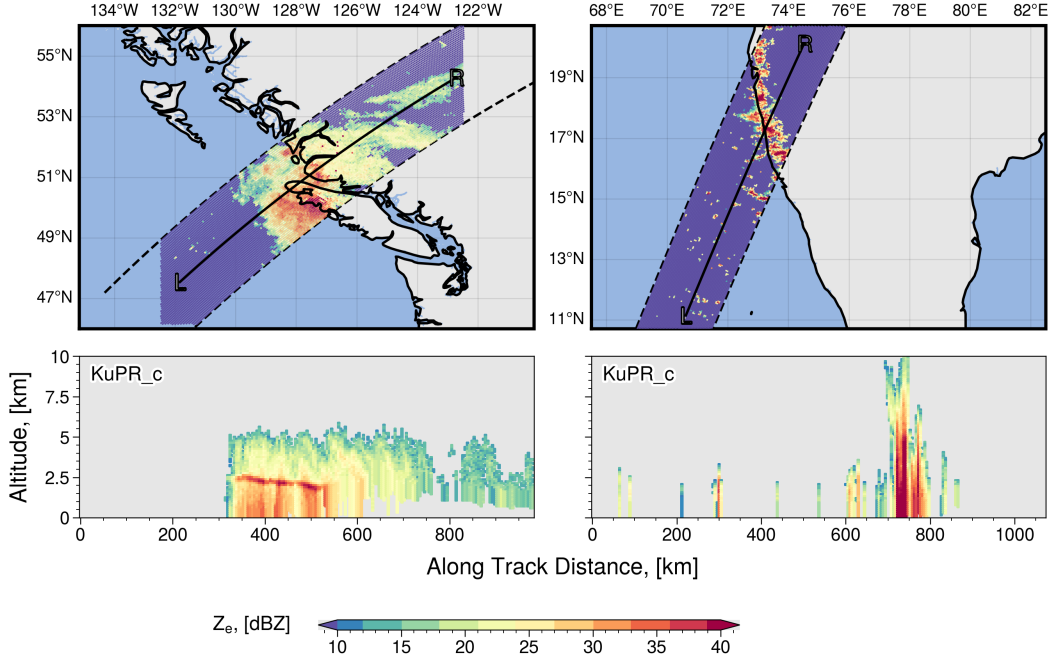


FIG. 2. Near-surface radar reflectivity from the Ku-band GPM radar (top) and vertical cross-section of corrected Ku-band reflectivity (bottom) for two overpasses : February 11th, 2015 (GPM orbit No. 005434) over the coast range of British Columbia (left) and June 19th, 2014 (GPM orbit No. 001735) over the Western Ghats (right). The black lines on the top panels show the location of the cross-sections on the bottom panels, with the L and R marks corresponding to the left/right of the cross-sections. This figure was produced using the DRpy software package (Chase and Syed 2022).

While wide radar echoes are also observed in the tropics, such as in mesoscale convective systems (Houze et al. 2015), such systems reach deeper heights than winter midlatitude storms (because the tropical troposphere is nearly moist neutrally stable (Xu and Emanuel 1989), while midlatitudes are more stably stratified, preventing convection embedded in midlatitude cyclones from reaching deep heights).

Tropical orographic precipitation has a more even temporal distribution than surrounding continental or oceanic precipitation (Van den Hende et al. 2021; Espinoza et al. 2015; Sobel et al. 2011). Nevertheless, intraseasonal and interannual variability in orographic rainfall seems to be influenced by the classical tropical modes that regulate moist convection. Examples include the boreal summer intraseasonal oscillation (BSISO, Shige et al. 2017; Hunt et al. 2021), the Madden-Julian Oscillation (MJO, Bagtasa 2020) and large-scale interannual modes such as the El Niño-Southern

95 Oscillation and the Indian Ocean Dipole (Yen et al. 2011; Revadekar et al. 2018; Lyon et al. 2006;
96 Smith et al. 2013). Hence, any successful theory for tropical orographic precipitation needs to
97 address the question of how mountains interact with moist convection.

98 Boundary-layer moist static energy and free-tropospheric temperature regulate moist convection
99 by influencing column stability. Observations and simulations have shown that free-tropospheric
100 water vapor also exerts a strong control on precipitation, consistent with the idea that entrainment
101 of free-tropospheric air modulates plume buoyancy (e.g., Derbyshire et al. 2004). Tropical rainfall
102 is thus jointly influenced by free-tropospheric temperature and moisture, and interacts with slower,
103 balanced dynamics to eliminate positive perturbations in these quantities—a behavior termed
104 lower-tropospheric quasi-equilibrium (QE, e.g., Raymond et al. 2015). The prominent role of lower-
105 tropospheric moisture has been confirmed in observations of orographic convection at low latitudes
106 (Hunt et al. 2021; Nelson et al. 2022). Beyond the lower-tropospheric thermodynamic environment,
107 factors such as the wind profile—especially vertical wind shear, which one could expect to be
108 important in the presence of mountain waves—should affect moist convective development (see,
109 e.g., Robe and Emanuel 2001; Anber et al. 2014; Peters et al. 2022a,b). We do not consider such
110 factors here.

111 Ahmed et al. (2020) cast the observed dependence of tropical convection on the lower-
112 tropospheric thermodynamic environment into a simple buoyancy-based framework. Precipitation
113 is strongly controlled by a measure of plume buoyancy that takes into account the influences of
114 instability and entrainment, and depends on boundary layer equivalent potential temperature as
115 well as lower-free-tropospheric temperature and moisture. We recently posited (Nicolas and Boos
116 2022, hereafter NB22) that mechanically forced orographic convection can be understood in this
117 framework, with stationary mountain waves disturbing lower-free-tropospheric thermodynamics,
118 in turn affecting precipitation. We developed a linear model for the spatial distribution of rainfall,
119 combining orographic gravity wave dynamics with the linearized QE closure of Ahmed et al.
120 (2020). That model assumes a simple background state that has horizontally uniform temperature
121 and moisture profiles, with horizontally and vertically uniform wind. At first order, the temperature
122 and moisture perturbations are dictated by vertical displacement in a mountain wave, which is in
123 turn controlled by the topographic shape, cross-slope wind, and static stability. The normalized
124 gross moist stability (e.g., Raymond et al. 2009) appears as a second-order control, because it mod-

ulates convective moisture relaxation. One goal of the present work is to evaluate to what extent this framework (extended to two horizontal dimensions) can explain observed spatial patterns of orographic tropical rainfall.

More generally, this study explores the physical drivers behind the temporal variations and spatial structure of orographic precipitation around six tropical mountain regions: the Western Ghats (India), the western coast of Myanmar (Arakan Yoma mountain range), the eastern coast of Vietnam (Annam Range), the Malay peninsula, the Philippines, and the island of New Britain (Papua New Guinea). We justify the use of a lower-tropospheric buoyancy measure in quantifying daily orographic precipitation variability and explore the dominant controls on its components—both within the boundary layer and the lower-free-troposphere. We then explore to what extent time-averages of this buoyancy measure account for observed spatial patterns of rainfall, and test the QE-based linear theory of NB22 against observations.

2. Data

Two precipitation products are used. Seasonal averages (used in sections 1, 3, and 6) are obtained from monthly averages of near-surface precipitation rates from the Tropical Rainfall Measuring Mission Ku-band precipitation radar (TRMM PR 3A25, Tropical Rainfall Measuring Mission 2021) for the 01/2001–03/2014 period and the Global Precipitation Measurement dual-frequency precipitation radar (GPM 3DPR, Iguchi and Meneghini 2021) for the 04/2014–12/2020 period, both on a 0.25° grid. In section 4, where we require daily resolution, we use the IMERG V06B precipitation dataset (Huffman et al. 2019), which combines satellite-based infrared and passive microwave measurements with rain gauge data to provide hourly estimates at 0.1° resolution. IMERG is known to suffer from biases in regions of complex topography relative to rain gauge measurements, but these biases are reduced when considering spatial averages (Pradhan et al. 2022). We use daily precipitation averages at large spatial scales, and the regions over which we average consist of 45%–80% ocean points, where confidence in IMERG retrievals is higher.

We evaluate the thermodynamic environment and horizontal winds from the ERA5 reanalysis (Hersbach et al. 2018), which provides hourly data at 0.25° resolution. Johnston et al. (2021) showed that moisture soundings from ERA5 had excellent agreement with satellite-based radio occultation retrievals in the tropics and subtropics. Proper evaluation of ERA5 lower-tropospheric

temperature is lacking; we note that Hersbach et al. (2020) showed improved 850 hPa temperature estimates (when compared to radiosondes) over ERA-Interim, especially in the past two decades.

Unless otherwise specified, we use topography from the ETOPO1 global relief model (National Geophysical Data Center 2011; Amante and Eakins 2008), at 60 arc-second resolution.

3. Selecting regions of mechanically forced tropical orographic rainfall

To illustrate the physical drivers of tropical orographic precipitation, we select six regions in South Asia and the Maritime Continent. We focus on mechanically forced convection, a regime in which orographic forcing is felt through the forced uplift of impinging flow, by opposition to thermal forcing, where the diurnal cycle of heating over sloped terrain drives low-level convergence. The wind speed threshold marking the transition from thermal to mechanical forcing depends on various factors including static stability N and mountain height h_m . One quantity often used to characterize orographic flows is the nondimensional mountain height¹, $M = Nh_m/U$, where U is the cross-slope wind speed. Flows with $M < 1$ tend to cross topography (rather than being blocked upstream), which may prevent the development of thermally forced circulations (Kirshbaum et al. 2018). For moderately high mountains (500–1000 m) in the tropics, various studies have suggested that mechanical forcing dominates above about 5 m s^{-1} (Nugent et al. 2014; Wang and Sobel 2017). Accordingly, we selected six regions with a mean upstream wind (during the local rainy season) higher than 5 m s^{-1} and a visible orographic rain band. This sample is not an exhaustive representation of tropical orographic rainfall, although we think it is quite representative of mechanically forced cases. These regions are outlined in Fig. 1, with close-up views of their topography and seasonal-mean rainfall and wind in Fig. 3. The rainfall maps have some visible noise because they are only based on TRMM and GPM radar overpasses, which have sparse temporal coverage.

For each region, we analyze data over a 20-year period (2001–2020) during the local雨季 (which also corresponds to a mechanically forced regime), defined below for each specific case. Two regions (Vietnam and the Philippines) experience a second rainfall peak in boreal summer on the other side of their mountain ranges, associated with reversed winds during the summer monsoon (see Fig. 1). Because the winds are not as strong then, the dominance of mechanical forcing cannot be clearly established, and we did not include these secondary rainy seasons in our analysis. In section 4, we analyze daily data averaged over the orographic rain bands;

¹ M is also the inverse of a Froude number.

TABLE 1. Key information about the regions studied. Here and in later tables, PNG refers to Papua New Guinea.

Region name	Rainy season considered in this study	Nondimensional mountain height
Western Ghats	June-August	0.8
Myanmar	June-August	0.8
Vietnam	October-November	1
Malaysia	November-December	0.5
Philippines	November-December	0.3
PNG	June-August	0.4

these rain bands are defined manually using rectangular boxes and outlined in red in Figure 3. We summarize key information about each region in Table 1, and describe these in detail hereafter.

Three of these regions have their雨iest season in boreal summer (June-August). The Western Ghats, a mountain range on the west coast of peninsular India, form a kilometer-high barrier to the southwesterly monsoon flow. With $M \approx 0.8$ (measuring wind speed 500 km upstream of the coast and 100 m above the surface to avoid influences from surface friction and flow deceleration by topography), the Ghats fall within a clear mechanically forced regime, as attested by the small diurnal cycle of rainfall there (Shige et al. 2017). The dynamics of orographic precipitation in the Western Ghats have been the subject of several modeling studies (Smith and Lin 1983; Grossman and Durran 1984; Ogura and Yoshizaki 1988; Xie et al. 2006; Oouchi et al. 2009; Sijikumar et al. 2013; Zhang and Smith 2018). These studies confirm that the presence of orography is crucial in producing the observed rain band, and (expectedly) that latent heating cannot be neglected in describing the orographic flow. Past literature has also discussed the location of the rainfall maximum upstream of the Western Ghats. While some studies initially suggested that it occurred upstream of the coastline (e.g., Xie et al. 2006), Shige et al. (2017) determined that it was positioned over the western slopes of the Ghats (consistent with Fig. 3).

The Arakan Yoma mountain range, located along the coast of Myanmar, also interacts with the Asian summer monsoon (Oouchi et al. 2009; Wu et al. 2018). With maximum seasonal-mean precipitation values exceeding 30 mm day^{-1} upstream of the range, it is responsible for the strongest rain band (in terms of mean precipitation rate) on Earth in boreal summer. This precipitation maximum is located along the coast (see Fig. 3 and Shige et al. 2017). Compared to the Western Ghats, convection is deeper and of wider scale upstream of Myanmar, a fact that

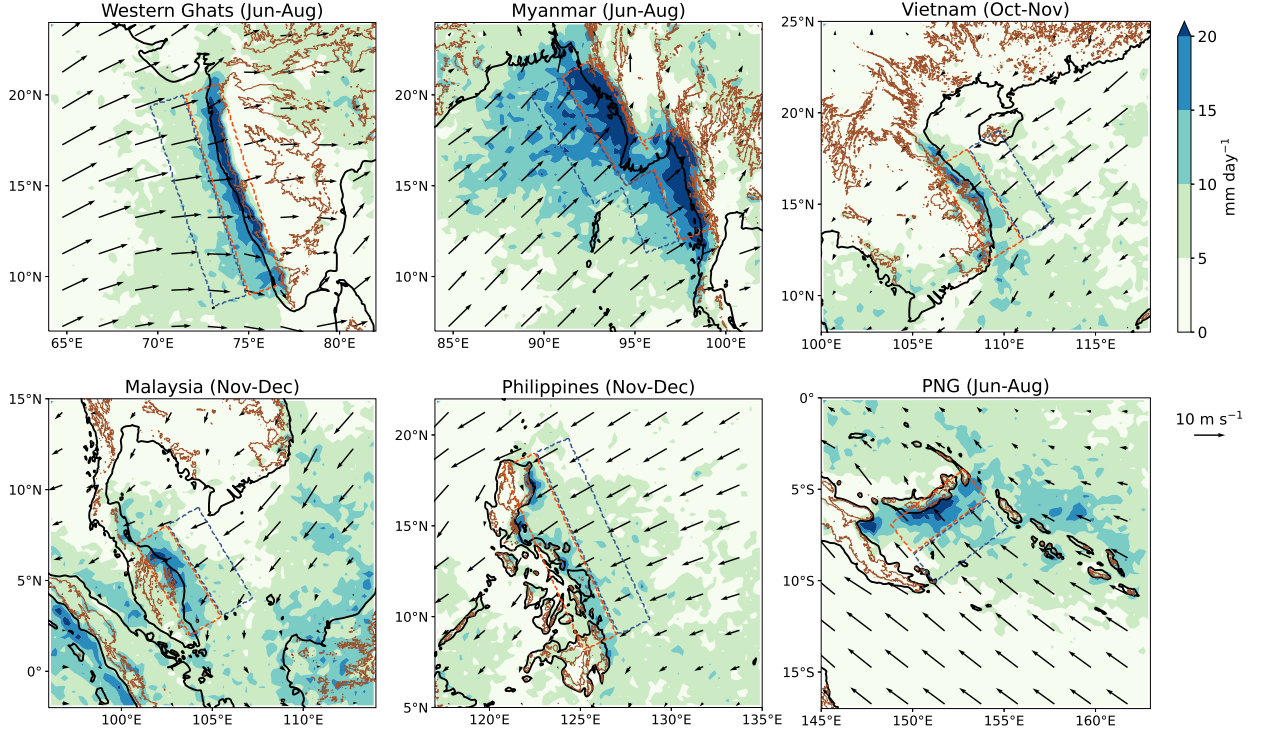
205 Shrestha et al. (2015) associated with differences in lower tropospheric humidity. M has a similar
206 value around 0.8 there.

207 The island of New Britain, in Papua New Guinea (hereafter PNG), is our third region of interest
208 in boreal summer. The mountains are of modest height there (300 m when averaging across the
209 island, although individual peaks exceed 2 km), but a strong precipitation band reaching 25 mm
210 day⁻¹ lies upstream of the island. Winds speeds around 8–9 m s⁻¹ yield a nondimensional mountain
211 height $M \simeq 0.4$. Orographic rainfall in PNG has been the focus of a few studies (e.g., Biasutti et al.
212 2012; Smith et al. 2013).

213 The remaining three regions are associated with boreal autumn rainfall. The coast of Vietnam,
214 east of the Annam range, receives most of its rainfall in October and November (Chen et al. 2012;
215 Ramesh et al. 2021), with an onshore cross-slope wind of 8–9 m s⁻¹ during this season ($M = 1$).
216 The eastern coast of the Philippines experiences a late autumn precipitation peak (November–
217 December) with a similar wind speed and $M = 0.3$ (Chang et al. 2005; Robertson et al. 2011).
218 Finally, the eastern half of the Malay Peninsula also receives most of its rainfall in November and
219 December (Chen et al. 2013), similarly associated with mechanical orographic forcing ($M = 0.5$).

225 4. Controls on daily variations of orographic rainfall

226 In the tropics, mechanically forced orographic rainfall is subject to less temporal variability than
227 rainfall over surrounding land and ocean. In particular, it has a weak diurnal cycle, as noted by
228 Shige et al. (2017) in the Western Ghats and in Myanmar (see also Aoki and Shige 2024). This
229 can be understood as resulting from daytime heating of the boundary layer being limited by the
230 ventilation resulting from strong wind (e.g., Nugent et al. 2014). The distribution of daily rainfall
231 within regions where mechanical forcing dominates is also more uniform, with less contribution
232 from extreme days. This was noted by Espinoza et al. (2015) in the Central Andes and is confirmed
233 for regions studied here (Table 2). Nevertheless, these regions still show substantial subseasonal
234 rainfall variations. The goal of this section is to determine the factors governing these temporal
235 variations of daily-mean precipitation.



220 FIG. 3. TRMM PR and GPM DPR near-surface precipitation, 500 m surface height level (thin brown contours),
221 and ERA5 wind vectors 100 m above the surface in six tropical regions, averaged over each region's雨季
222 (see text) from 2001 to 2020. The red dashed boxes outline the orographic rain bands, which are analyzed
223 in section 4. The blue dashed boxes define the regions over which cross-slope IVT is averaged in Fig. 5. Here
224 and in later figures, PNG refers to Papua New Guinea.

236 TABLE 2. Percentage of seasonal rainfall contributed by the rainiest days (defined as days and locations where
237 rainfall is above the 90th percentile), in the whole region and within the orographic rain band, for each region
238 studied. The rain bands are defined by the red dashed rectangles in Fig. 3.

Region name	Whole region	Orographic rain band
Western Ghats	74	53
Myanmar	59	43
Vietnam	80	73
Malaysia	63	61
Philippines	76	66
PNG	70	55

239 *a. Dynamic and thermodynamic predictors of daily rainfall variations*

240 The canonical picture of orographic rainfall highlights the importance of the cross-slope vapor
241 transport in governing rain rates (Smith 2019). In a saturated atmosphere ascending with velocity
242 w , the column-integrated condensation rate is

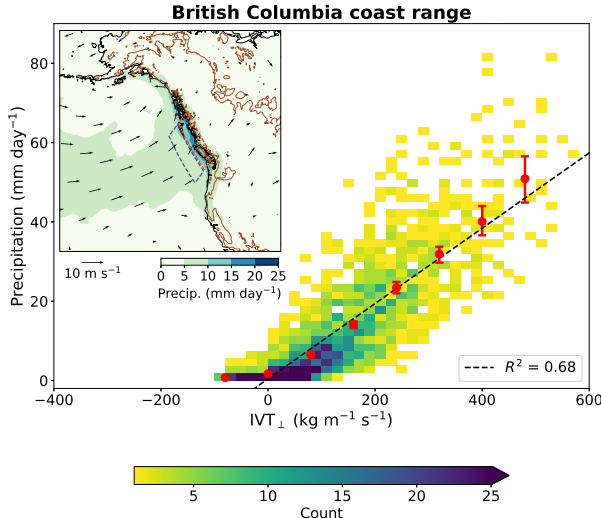
$$C = - \int_0^\infty w \frac{d(\rho q_{\text{sat}})}{dz} dz. \quad (1)$$

243 The water vapor density can be approximated as decreasing exponentially with z , with a scale height
244 H_{sat} . If \mathbf{u} denotes the surface horizontal wind and h the surface height, then $w(z=0) = \mathbf{u} \cdot \nabla h$. In
245 the simplest approximation where w is vertically uniform, then

$$C = \int_0^\infty (\mathbf{u} \cdot \nabla h) \frac{\rho q_{\text{sat}}}{H_{\text{sat}}} dz \simeq \frac{\text{IVT} \cdot \nabla h}{H_{\text{sat}}}, \quad (2)$$

253 where **IVT** denotes the vertically integrated water vapor transport. Setting precipitation equal to
254 the product of C with a precipitation efficiency, one sees that in this so-called upslope model,
255 it is proportional to the cross-slope IVT. This model has several shortcomings, including the
256 assumption of a saturated atmosphere and the oversimplified vertical velocity parameterization.
257 Nevertheless, it skillfully characterizes temporal rainfall variations in some midlatitude mountain
258 ranges, as illustrated for the British Columbia coastal range in Fig. 4; despite some scatter, daily
259 precipitation rates in winter are decently described by a linear relationship with cross-slope IVT
260 (hereafter IVT_{\perp}). Although the vertically uniform ascent model for vertical velocity ($w = \mathbf{u} \cdot \nabla h$)
261 is crude, it captures the simple fact that vertical velocities in convectively stable orographic flows
262 are controlled by cross-slope wind. Deviations from this simple picture, including effects of
263 stratification, wind shear, and the specific dynamics of various types of weather systems, yield the
264 scatter.

273 In the tropics, where convective ascent is more important, one might expect other factors than
274 cross-barrier winds to modulate ascent rates. Still, Bagtasa (2020) suggested that enhanced cross-
275 slope winds in the Philippines associated with certain phases of the MJO favored rainfall in late
276 autumn. Similarly, Shige et al. (2017) showed that rainfall in the Western Ghats and the Arakan
277 Yoma range of Myanmar was in phase with the southwesterly wind strength modulated by the
278 BSISO. This suggests that cross-slope winds, and perhaps cross-slope IVT, still are important

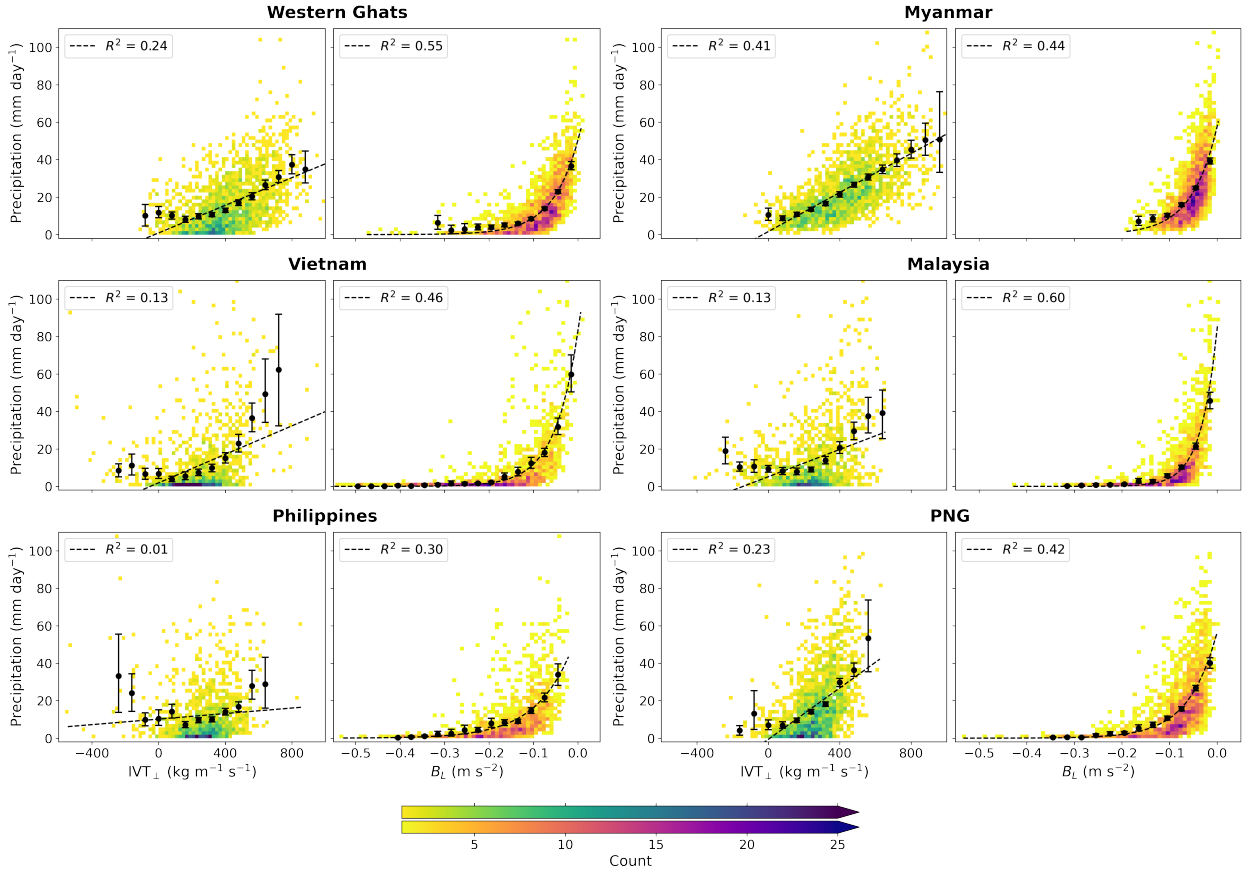


246 FIG. 4. Joint distributions of daily cross-slope IVT and precipitation in the coast range of British Columbia.
 247 Precipitation is averaged over the orographic rain band (red box in the inset). Cross-slope IVT (defined as its
 248 northeastward component) is averaged immediately upstream of the precipitation maximum (blue dashed box
 249 in the inset). The black dashed line shows the best linear fit. The red dots represent conditionally averaged
 250 precipitation over bins of width $80 \text{ kg m}^{-1} \text{s}^{-1}$, with error bars representing a 95% confidence interval obtained by
 251 bootstrapping. The inset shows climatological rain (IMERG) and 100 m wind (ERA5) averaged over November-
 252 January.

253 controls on orographic precipitation at low latitudes. Figure 5 (first and third columns) shows the
 254 joint distributions of IVT_\perp and precipitation, as well as precipitation conditionally averaged on
 255 IVT_\perp^2 . While a positive relationship remains, it does not hold as strongly as in the midlatitude
 256 winter case shown in Fig. 4, with numerous dry days associated with strong IVT_\perp . Therefore, we
 257 attempt to find another variable to characterize temporal variations in tropical orographic rainfall,
 258 starting with thermodynamic metrics that have been associated with convective rainfall.

259 The question of what environmental factors set convective precipitation rates is at the heart of
 260 any theory of tropical atmospheric dynamics. The QE hypothesis (e.g., Emanuel et al. 1994) states
 261 that convection acts to deplete anomalies in convective available potential energy (CAPE). This
 262 description predicts the effect moist convection has on its environment, consuming instability and
 263 setting vertical temperature profiles close to moist adiabats. However, it alone does not provide

²Throughout this manuscript, conditionally averaging A on B means averaging A over days where B is in a given range of values. Where relevant, the ranges of values are defined in the figure captions.



265 FIG. 5. Joint distributions of daily cross-slope IVT and precipitation (first and third columns, green colors)
266 and B_L and precipitation (second and fourth columns, red colors). B_L and precipitation are averaged spatially
267 over the rain band regions (red boxes in Fig. 3). IVT is averaged right upstream of the rain band regions (blue
268 boxes in Fig. 3). The cross-slope direction is defined as 70° (Ghats), 60° (Myanmar), 240° (Vietnam), 225°
269 (Malaysia), 225° (Philippines), and 320° (PNG). Linear fits (for the IVT-precipitation relation) and exponential
270 fits (for the B_L -precipitation relation) are shown as dashed lines, with the associated coefficients of determination
271 in the legend. The black dots represent conditionally averaged precipitation over bins of width $80 \text{ kg m}^{-1}\text{s}^{-1}$ (for
272 IVT) and 0.03 m s^{-2} (for B_L), with error bars representing a 95% confidence interval obtained by bootstrapping.

290 information on convective intensity or precipitation rates, given environmental conditions. One
291 further development stems from the observed exponential dependence of precipitation rates on
292 column moisture content (e.g., Bretherton et al. 2004). The physical roots of this dependence lie
293 in the effect that entrainment of free-tropospheric air has on plume buoyancy.

294 Seeking a unified measure that would characterize rainfall across the tropics, Ahmed and Neelin
 295 (2018) derived an expression for a lower-tropospheric averaged plume buoyancy, that only depends
 296 on environmental temperature and moisture profiles. Dividing the lower atmosphere in two layers,
 297 a boundary layer (subscript B) and a lower-free-troposphere³ (subscript L), this expression reads
 298 (Ahmed et al. 2020)

$$B_L = g \left[\alpha_B \frac{\theta_{eB} - \theta_{eL}^*}{\theta_{eL}^*} - \alpha_L \frac{\theta_{eL}^* - \theta_{eL}}{\theta_{eL}^*} \right], \quad (3)$$

299 where g is the acceleration of gravity, θ_e is equivalent potential temperature (and θ_e^* its saturated
 300 value), and subscripts denote averages taken over respective layers. The weights α_B and $\alpha_L = 1 - \alpha_B$
 301 depend on the thickness of each layer and the assumed mass flux profile of the plume. We use
 302 $\alpha_B = 0.52$ (as in Ahmed et al. 2020). The first term in (3) is a CAPE-like term, wherein the
 303 difference between boundary layer θ_e and lower-free-tropospheric θ_e^* provides a measure of moist
 304 convective instability. The second term describes subsaturation of the lower free troposphere,
 305 and quantifies the efficiency of entrainment at reducing buoyancy by drying the plume (hence the
 306 negative sign in front of it).

316 When conditionally averaged on B_L (at $O(10$ km) and hourly scale), precipitation is near-zero
 317 for negative values and strongly increases above zero buoyancy, a behavior reminiscent of its expo-
 318 nential dependence on column moisture. The strength of this precipitation-buoyancy relationship
 319 lies in its universality, as it holds over all tropical oceans, and, with slight modifications, over
 320 tropical land (Ahmed et al. 2020). Using conditional averages reduces the scatter in precipitation
 321 rates associated with a given value of B_L . This spread can be due to both stochasticity or ignored
 322 physical effects, e.g., higher-order dependencies on the vertical structure of environmental temper-
 323 ature and moisture, or wind shear effects. Figure 5 (second and fourth columns), shows the joint
 324 distribution of precipitation and B_L for each region, using daily-mean data spatially averaged over
 325 the rain bands (red boxes in Figure 3). Spatially averaging the nonlinear rainfall- B_L relationship
 326 is expected to smooth out the sharp increase around zero buoyancy; hence, we show exponential
 327 fits (rather than ramp fits of the form $\max(0, aB_L + b)$) with the joint distributions. We also show
 328 conditional averages at various B_L values. B_L is more skillful than IVT_\perp at capturing daily rainfall

³Here, the boundary layer is defined as between the surface and 900 hPa, and the lower-free-troposphere between 900 hPa and 600 hPa. We chose these definitions (over using a fixed-depth boundary layer and variable-depth lower free troposphere) so that lower-free-tropospheric averages are not affected by surface elevation changes. Points where the surface pressure is lower than 900 hPa are masked out of all analyses. These represent a small fraction of each domain, and can be visualized as the white shaded regions in Figure 11. The analyses are robust to the exact definition of the boundary layer top: changing it to 875 or 925 hPa does not significantly affect any of the results presented. Moreover, daily variations in boundary layer height (as determined by ERA5) are modest in the rain bands analyzed in Figs. 5–10, with standard deviations lower than 15 hPa.

variations in all regions except perhaps Myanmar, where the range of B_L is narrower than in other regions (during the summer monsoon, the coast of Myanmar is in a precipitating state most of the time). It is notable that B_L characterizes rainfall with similar accuracy in regions that have different convective vertical structures (Kumar and Bhat 2017; Shige and Kummerow 2016). This indicates that B_L is not only suitable to quantify rainfall from deep convection, but that it is also an adequate measure in regions where precipitation tops frequently lie around 4 to 6 km. We next decompose variations in B_L into contributions from its components to understand the origins of precipitation variability in tropical orographic regions.

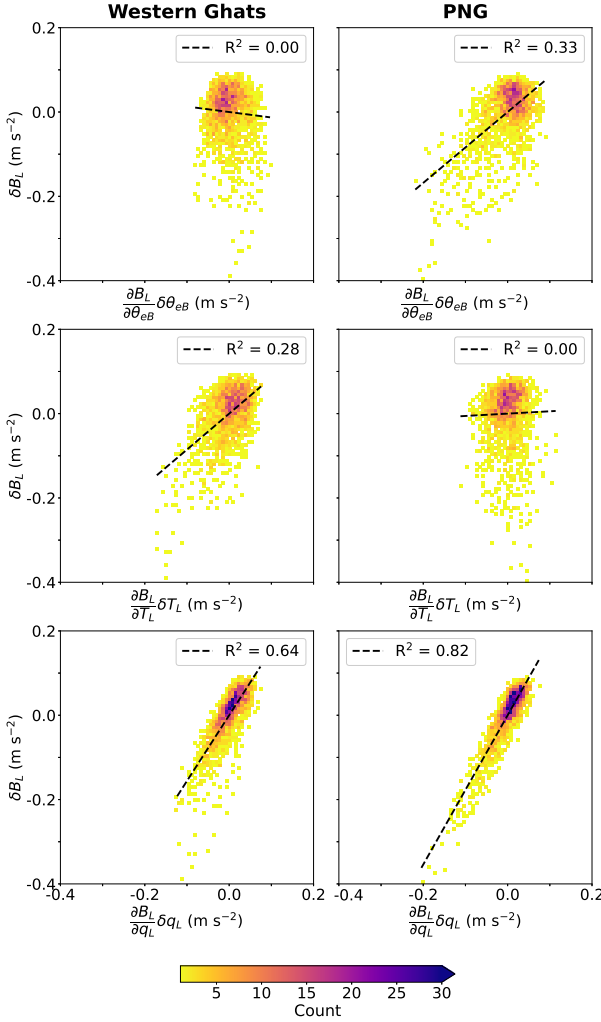
B_L is a function of three variables: θ_{eB} , θ_{eL} , and θ_{eL}^* (eqn. 3). Alternatively, following Ahmed et al. (2020), it can be viewed as a function of θ_{eB} , T_L and q_L , where T is temperature and q denotes specific humidity, hereafter in temperature units (i.e. multiplied by the ratio of the latent heat of vaporization of water L_v to the heat capacity of air at constant pressure c_p). In this description, plume buoyancy is affected by boundary layer θ_e (which affects lower-tropospheric stability), lower-free-tropospheric temperature (affecting both stability and lower-free-tropospheric subsaturation) and lower-free-tropospheric moisture (affecting only the subsaturation component).

To evaluate the sensitivity of B_L to each component, we linearize its expression:

$$\delta B_L = \frac{\partial B_L}{\partial \theta_{eB}} \delta \theta_{eB} + \frac{\partial B_L}{\partial T_L} \delta T_L + \frac{\partial B_L}{\partial q_L} \delta q_L \quad (4)$$

where δ denotes a deviation from a time-average, $\partial B_L / \partial \theta_{eB} = g \alpha_B / \theta_{eL}^*$, and the expressions for $\partial B_L / \partial T_L$ and $\partial B_L / \partial q_L$ are given in Ahmed et al. (2020) (these expressions were derived from a simplified version of B_L that is very close to the one employed here). Here, we use fixed values of $\partial B_L / \partial \theta_{eB} = 0.014$, $\partial B_L / \partial T_L = -0.058$, and $\partial B_L / \partial q_L = 0.014$, which have little dependence on the specific base state considered.

Figure 6 examines the contribution of each term on the right-hand-side of (4) to variations in B_L , over the Western Ghats and PNG. For example, to estimate the contribution of θ_{eB} variations to B_L variations, we fix T_L and q_L and estimate the B_L perturbations that would have occurred if only θ_{eB} had varied, i.e. $(\partial B_L / \partial \theta_{eB}) \delta \theta_{eB}$. We regress δB_L on this measure and show the joint distribution of both quantities (top panels), then repeat the same analysis with $(\partial B_L / \partial T_L) \delta T_L$ (middle panels) and $(\partial B_L / \partial q_L) \delta q_L$ (bottom panels). It is apparent from these univariate linear regressions that q_L dominates B_L variations in both regions. This is true even though B_L is



307 FIG. 6. Joint distributions of buoyancy anomalies δB_L and their contribution from θ_{eB} anomalies (first row), T_L
 308 anomalies (second row), and q_L anomalies (third row), for two regions illustrating different regimes: the Western
 309 Ghats (left) and PNG (right). For each plot, δB_L is also regressed on the individual contribution $(\partial B_L / \partial V) \delta V$
 310 where $V = \theta_{eB}, T_L$, or q_L . Black dashed lines show the best fit linear regression.

357 four times more sensitive to T_L ($|\partial B_L / \partial T_L| \simeq 4 \partial B_L / \partial q_L$). Indeed, variations of q_L are less
 358 constrained than those of T_L : lower-free-tropospheric temperature anomalies are quickly smoothed
 359 in the tropics by gravity waves, resulting in a state of weak temperature gradients (e.g., Sobel
 360 et al. 2001). Over the Western Ghats, T_L variations still account for 28% of the variance in B_L ,
 361 while θ_{eB} variations do not correlate with B_L . In PNG, the converse picture holds. Figure 7
 362 shows the coefficients of determination (R^2) of the regression lines that appear in Fig. 6, extended
 363 to all regions. In addition, we perform bivariate linear regressions of δB_L against θ_{eB} and T_L ,

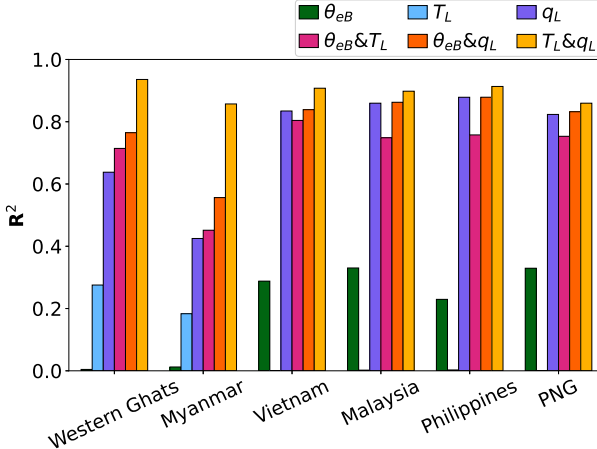


FIG. 7. Coefficients of determination (R^2) from linear regressions of δB_L against its individual contributions from θ_{eB} , T_L , and q_L anomalies (see Fig. 6), as well as joint contributions from pairs of these variables. Note that despite differences in the univariate R^2 's across regions (with θ_{eB} anomalies accounting for more variance in B_L than T_L anomalies in a univariate sense), the (T_L, q_L) pair explains the highest fraction of variance in δB_L in all regions.

θ_{eB} and q_L , and T_L and q_L (we omit $\partial B_L / \partial \theta_{eB}$ and other prefactors as these only change the regression coefficients, and not the R^2). From the univariate regressions alone, there seem to be two types of behavior: one where buoyancy variations are controlled by lower-free-tropospheric thermodynamic quantities (the Western Ghats and Myanmar), and the other where boundary layer θ_e and lower-free-tropospheric moisture set these variations (Vietnam, Malaysia, the Philippines, and PNG). However, the bivariate regressions show that in all regions, T_L and q_L account together for the highest fraction (over 85%) of the variance in B_L . Consistently, the rest of this section focuses primarily on the factors governing T_L and q_L variations.

An important caveat is that the three variables that control variations in lower tropospheric buoyancy B_L are not independent of each other. In QE theory, convection rapidly reduces CAPE variations, tying free-tropospheric saturation equivalent potential temperature θ_e^* to subcloud layer equivalent potential temperature θ_{eB} . Thus, one expects θ_{eB} and T_L to exhibit substantial correlation. Indeed, correlation coefficients between daily θ_{eB} and T_L averaged over the orographic precipitation bands vary between 0.7 and 0.9 in all regions. However, this relationship only indicates that θ_{eB} and θ_{eL}^* covary, and does not provide insight on B_L variations because B_L depends on $\theta_{eB} - \theta_{eL}^*$, as in (3). Additionally, turbulent exchange between the subcloud layer and the lower

389 TABLE 3. Correlations between daily precipitation (P) and the three quantities affecting plume buoyancy (θ_{eB} ,
 390 T_L and q_L), and between daily SST and boundary layer equivalent potential temperature θ_{eB} . Precipitation, θ_{eB} ,
 391 T_L and q_L are averaged over the red boxes in Fig. 3, and SST is averaged over the ocean part of each box.

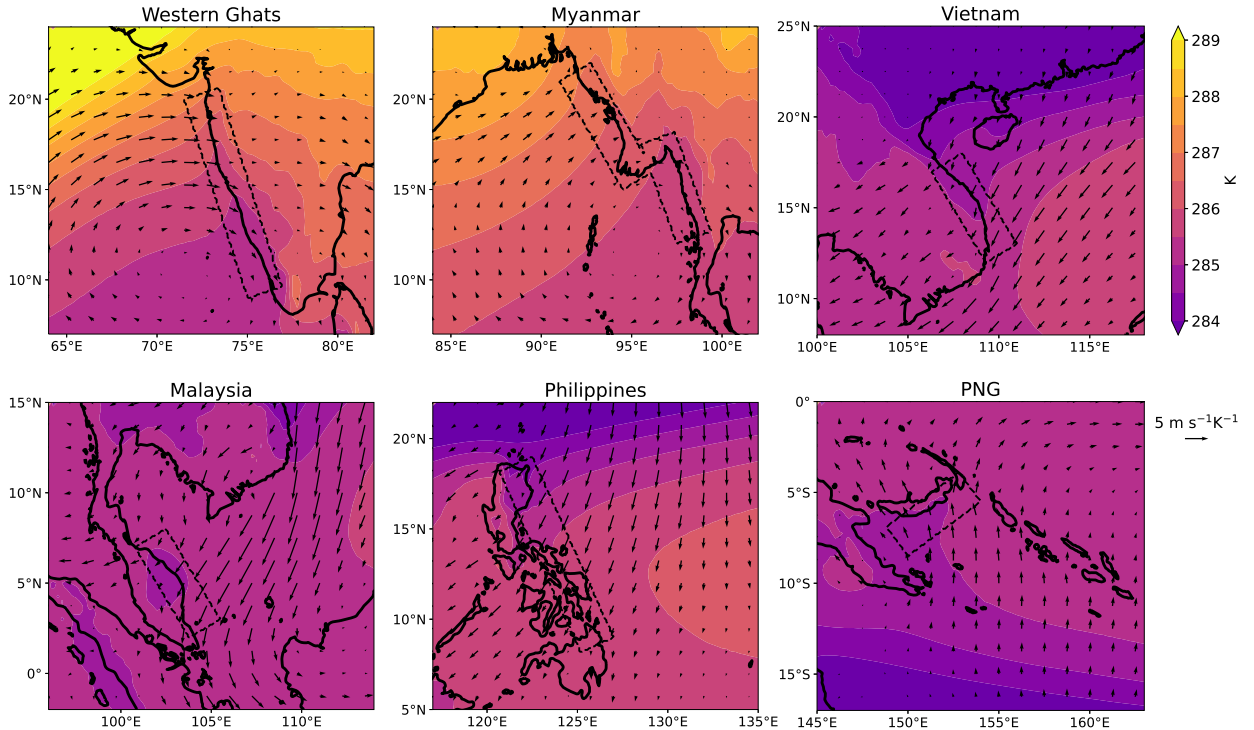
Region name	P - θ_{eB}	P - T_L	P - q_L	SST- θ_{eB}
Western Ghats	0.19	-0.15	0.56	0.80
Myanmar	0.16	-0.18	0.30	0.53
Vietnam	0.23	0.03	0.53	0.61
Malaysia	0.17	-0.18	0.51	0.69
Philippines	0.12	-0.06	0.50	0.56
PNG	0.15	-0.15	0.51	0.60

380 free troposphere produces smaller correlations (0.3–0.6) between daily θ_{eB} and q_L variations. T_L
 381 and q_L are essentially uncorrelated across all regions.

382 To link this analysis back to precipitation variations, we compute correlations between daily
 383 values of rainfall and each of θ_{eB} , T_L , and q_L upstream of each of the mountain ranges studied
 384 (Table 3). These correlations are only a crude measure of the association of each component
 385 with precipitation, given that the precipitation-buoyancy relationship is expected to be nonlinear.
 386 Nevertheless, a few of the observations made above hold: q_L has the strongest association with
 387 precipitation, T_L anomalies are negatively associated with precipitation (recall that $\partial B_L / \partial T_L < 0$),
 388 and θ_{eB} has a weak positive association with rainfall.

392 b. Controls on daily θ_{eB} variations

393 In this work, the boundary layer extends between the 900 hPa level and the surface—which
 394 loosely corresponds to the subcloud layer. Boundary layer θ_e , or equivalently subcloud entropy, is
 395 set by exchanges with the surface and the lower free troposphere, with a small contribution from
 396 radiative cooling (Emanuel et al. 1994). Entropy exchanges at the top of the boundary layer are
 397 twofold: one contribution being in the form of quasi-continuous turbulent mixing across the top of
 398 the layer, the other one arising from penetrative convective downdrafts. Over ocean, sea-surface
 399 temperature (SST) is often the dominant quantity affecting subcloud entropy (e.g., Lindzen and
 400 Nigam 1987). Because the orographic rain bands of interest in this section are in close proximity
 401 to the sea, one might expect SSTs to exert a strong control on θ_{eB} . We verify this fact in Table 3:



408 FIG. 8. Boundary layer horizontal wind regressed on lower-free-tropospheric temperature (T_L , averaged in
 409 the dashed boxes). The result is multiplied by -1 so that upslope flow is associated with negative temperature
 410 perturbations. The color shading shows seasonal-mean T_L . Arrows are masked where neither the u wind
 411 regression nor the v wind regression satisfy the false discovery rate criterion (Wilks 2016) with $\alpha = 0.01$.

402 SST strongly correlates with θ_{eB} at the daily scale, with correlation coefficients between 0.5 and
 403 0.8 in all regions.

404 Other factors such as surface wind speed variations or convective downdrafts contribute to
 405 variations in θ_{eB} on shorter timescales than SST changes. Because there is no clear influence of
 406 orographic mechanical forcing on any of these factors, we do not delve deeper into this topic.

407 *c. Controls on daily lower-free-tropospheric temperature variations*

408 Topographically forced gravity waves carry temperature perturbations. In the canonical picture
 409 of mechanical orographic forcing, a mountain of height h_m is placed in a stratified atmosphere (with
 410 buoyancy frequency N) with a uniform background horizontal wind U . When the nondimensional
 411 mountain height $Nh_m/U \lesssim 1$, the flow ascends over the mountain, creating (by adiabatic cooling)
 412 a cold anomaly in the lower-free-troposphere upstream. The stronger the wind, the deeper the

⁴¹⁷ ascent region, hence the colder the anomaly. In the case of an idealized ridge of height 1 km, the
⁴¹⁸ sensitivity of the temperature perturbation to the impinging wind is (see Appendix)

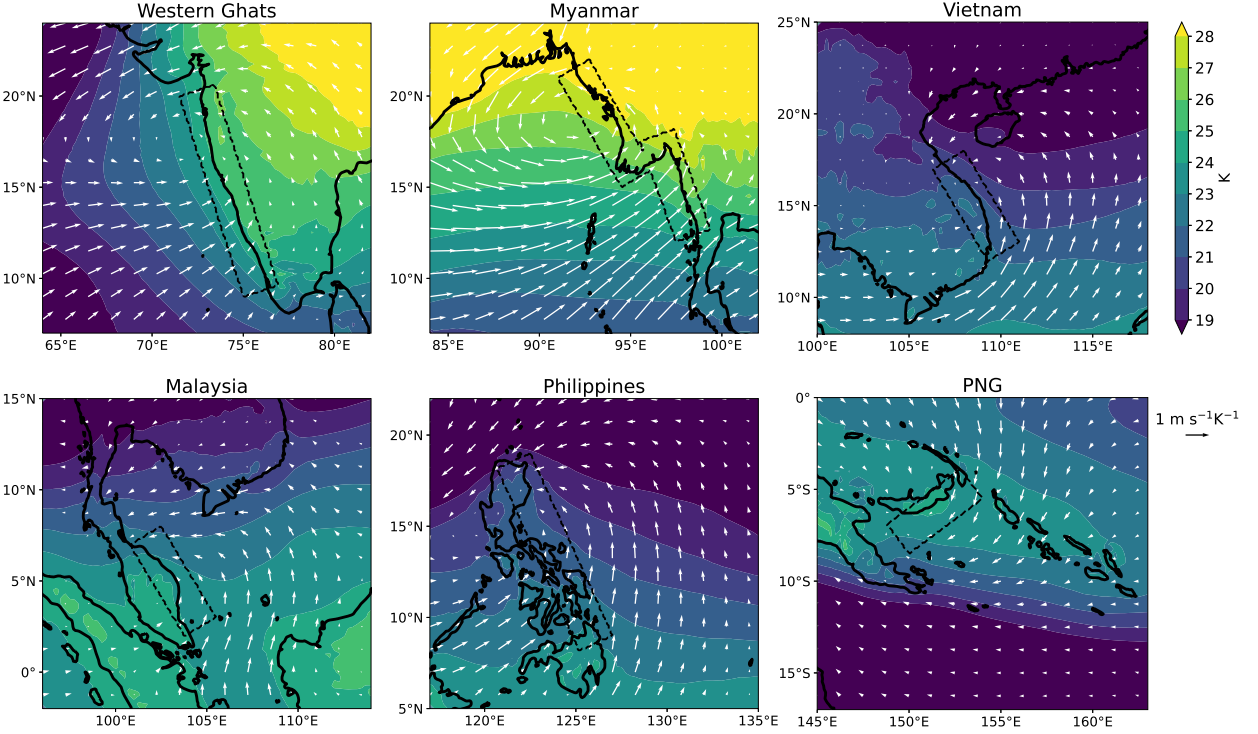
$$\frac{\partial T'_L}{\partial U} \simeq -0.2 \text{ K/(m s}^{-1}\text{)}. \quad (5)$$

⁴¹⁹ We now seek to verify whether T_L variations in our regions have patterns that are consistent with
⁴²⁰ this picture. Figure 8 shows time-mean T_L maps in all six regions. Cold anomalies (of around
⁴²¹ 0.5 K) are visible in each region’s rain band, indicated by poleward (in the Western Ghats and
⁴²² Myanmar) or equatorward (in Vietnam, the Philippines and PNG) excursions of isotherms upstream
⁴²³ of and above the topography. These anomalies are consistent with the idea of upstream cooling
⁴²⁴ by orographic lifting in the mean state. To study temporal variations in the strength of this cool
⁴²⁵ anomaly, we average T_L upstream of each mountain range to obtain daily timeseries. Because the
⁴²⁶ mountains are of modest height in each region, we expect mountain waves to be dominantly affected
⁴²⁷ by winds in the lowermost kilometer of the troposphere. We thus average horizontal winds within
⁴²⁸ the boundary layer and regress them on the T_L timeseries at each location. The resulting wind
⁴²⁹ vectors are multiplied by -1 so that onshore cross-slope flow corresponds to negative temperature
⁴³⁰ perturbations, and shown in Fig. 8. If our simple estimate (5) were to hold, regressed winds would
⁴³¹ have a magnitude around $5 \text{ m s}^{-1}\text{K}^{-1}$ for a 1 km-high mountain.

⁴³⁵ The wind regressions are directed onshore and cross-slope in each region, which is again consis-
⁴³⁶ tent with the idea that T_L is modulated by the strength of stationary mountain waves. Furthermore,
⁴³⁷ the magnitude of the regression vectors upstream of each region (except Myanmar) is around 2–5 m
⁴³⁸ $\text{s}^{-1}\text{K}^{-1}$, consistent with (5). It is apparent from Fig. 8 (especially in the Philippines, Vietnam, and
⁴³⁹ PNG) that cold anomalies are also associated with up-temperature-gradient winds: background
⁴⁴⁰ temperature gradients are not everywhere small in these tropical regions, and accordingly cooling
⁴⁴¹ can happen through horizontal advection.

⁴⁴² *d. Controls on daily lower-free-tropospheric moisture variations*

⁴⁴³ Given the dominant control q_L exerts on lower tropospheric buoyancy (Fig. 6), understanding
⁴⁴⁴ drivers of its temporal changes is key to understanding rainfall variations. In the same way
⁴⁴⁵ they bear temperature anomalies, mountain waves carry moisture perturbations through vertical
⁴⁴⁶ displacements in a background profile of specific humidity. Rising air upstream of a mountain



432 FIG. 9. Boundary layer horizontal wind regressed on lower-free-tropospheric moisture (q_L , averaged in the
 433 dashed boxes, in temperature units). The color shading shows seasonal-mean q_L . Arrows are masked using the
 434 same criterion as in Fig. 8.

447 moistens the lower-free-troposphere, while downstream subsidence dries it. The magnitude of this
 448 effect is estimated using linear mountain wave theory in the Appendix. In this idealized picture,
 449 the sensitivity of the upstream moisture perturbation to the cross-slope wind is

$$\frac{\partial q'_L}{\partial U} \simeq 0.5 \text{ K}/(\text{m s}^{-1}). \quad (6)$$

450 Once again, this effect neglects any convective response: mountain-induced T_L and q_L perturbations
 451 result in enhanced convection, which, in turn, dries the troposphere. A framework to understand
 452 the response of convection to thermodynamic perturbations in a mountain wave is presented in
 453 section 6. Solving for q'_L in this framework reduces the sensitivity in (6) by about half.

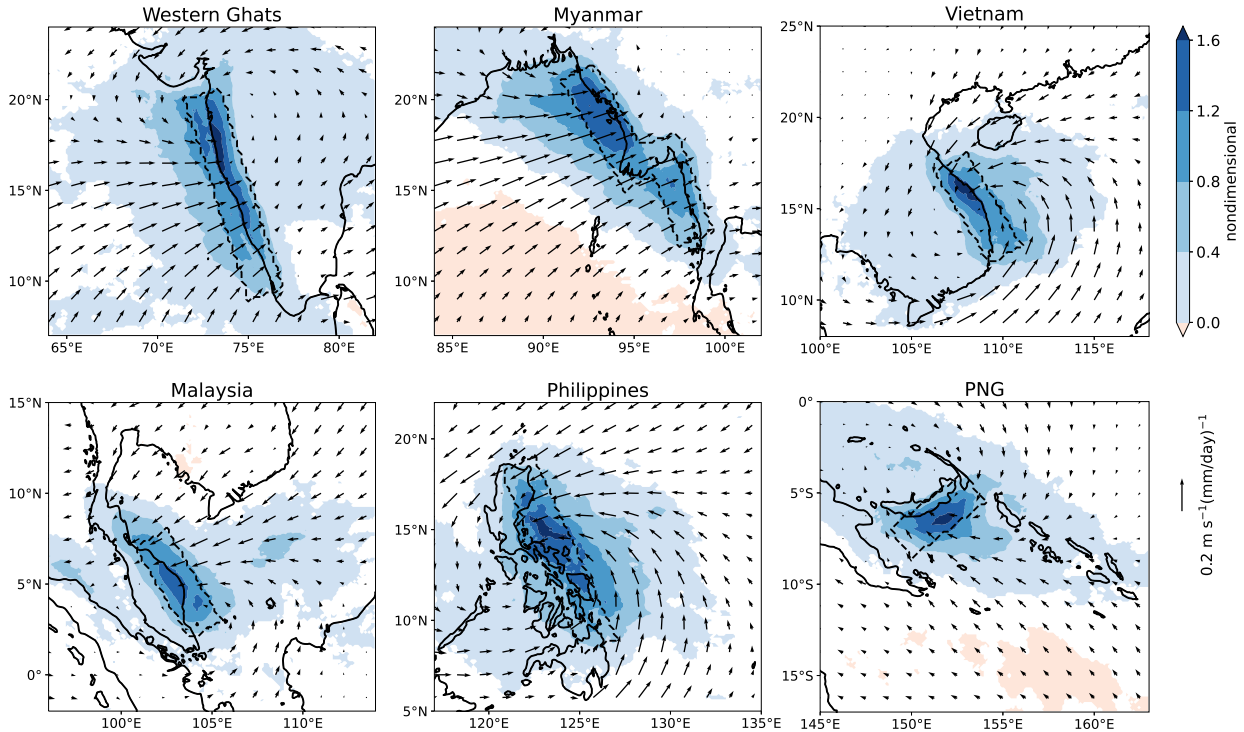
454 In the absence of horizontal gradients in the background moisture profile, q_L perturbations
 455 would be dominantly due to the time-mean ascent perturbation imposed by the terrain, which
 456 is well described by stationary mountain waves for a mechanically forced regime (NB22). In

457 Earth's tropics however, water vapor is far from horizontally homogeneous. This is apparent in
458 Fig. 9, where color shading represents the time-mean q_L in each region: horizontal moisture
459 gradients are much stronger than T_L gradients. Although the impact of orography on the mean q_L
460 distribution is less apparent compared to T_L (because of the stronger background q_L variations),
461 it seems to be associated with moisture contours deviating southward in Myanmar and northward
462 in the Philippines (corresponding to positive anomalies); a local maximum is also present over
463 PNG. Given the background horizontal moisture gradients and the moisture perturbations around
464 orography in Fig. 9, one might expect variations in q_L to be influenced by both winds along the
465 background moisture gradient and winds across orographic slopes.

466 The vectors in Fig. 9 show horizontal winds regressed on upstream-averaged q_L . In the Western
467 Ghats and Myanmar, moist perturbations are mostly associated with cross-slope winds, following
468 the theoretical picture of mechanical forcing. The magnitude of the regressions ($1\text{--}2 \text{ m s}^{-1}\text{K}^{-1}$) is
469 somewhat smaller than expected from (6); one would expect $2\text{--}4 \text{ m s}^{-1}\text{K}^{-1}$ when accounting for
470 the correction due to convective feedback (see above). The fact that both negative T_L and positive
471 q_L perturbations—hence positive B_L perturbations—are favored by cross-slope winds in the Ghats
472 and Myanmar explains why IVT_\perp characterizes precipitation better there than in other regions
473 (Fig. 5).

474 In Vietnam, Malaysia, and the Philippines, regressed winds have little cross-slope flow compo-
475 nent: they are mostly directed down mean moisture gradients. In these regions, moistening of the
476 lower free troposphere thus seems to be more effectively attained through large-scale horizontal
477 moisture advection than mechanical forcing of upslope flow. This result contrasts with the intu-
478 itive view that mechanically forced orographic precipitation and accompanying lower-tropospheric
479 humidity variations are mostly controlled by forced ascent, i.e. by the strength of upslope flow.
480 It shows that, despite its importance in setting the time-mean rainfall pattern, orographic forcing
481 might be less important than large-scale horizontal moisture advection in setting the daily vari-
482 ability of precipitation in these regions. Such control of precipitation by large-scale advection of
483 moisture in the midtroposphere was noted over the Arabian sea during the summer monsoon (Hunt
484 et al. 2021), and in northern Australia during its monsoon season (Xie et al. 2010).

485 The regression pattern in PNG is neither cross-slope nor down-moisture-gradient. Indeed, the
486 orographic rain band of PNG corresponds to a local maximum in lower-tropospheric specific



496 FIG. 10. Boundary layer horizontal wind regressed on precipitation averaged in the dashed boxes. The color
 497 shading shows precipitation regressed on this same index. Masked arrows and white shading indicate that the
 498 regressions do not satisfy the false discovery rate criterion with $\alpha = 0.01$.

487 humidity. Although we do not have a precise explanation for this pattern of wind anomalies, one
 488 may speculate that it is associated with large-scale upward motion in the South Pacific convergence
 489 zone (SPCZ), where PNG is located.

490 We note that moistening of the lower troposphere is not solely controlled by horizontal winds, and
 491 that any source of uplift, such as convectively coupled waves or cyclonic disturbances, will affect
 492 q_L . In this section we focused on horizontal wind control because horizontal winds dictate the
 493 strength of uplift in stationary mountain waves, and are consequently a primary factor modulating
 494 the effect of orography on q_L variations.

495 *e. Controls on daily precipitation variations*

499 To verify whether the same factors that govern lower-free-tropospheric temperature and moisture
 500 control rainfall variations, we now regress horizontal wind on daily upstream precipitation in each
 501 region (Fig. 10; upstream precipitation is defined as an average over the same boxes we previously

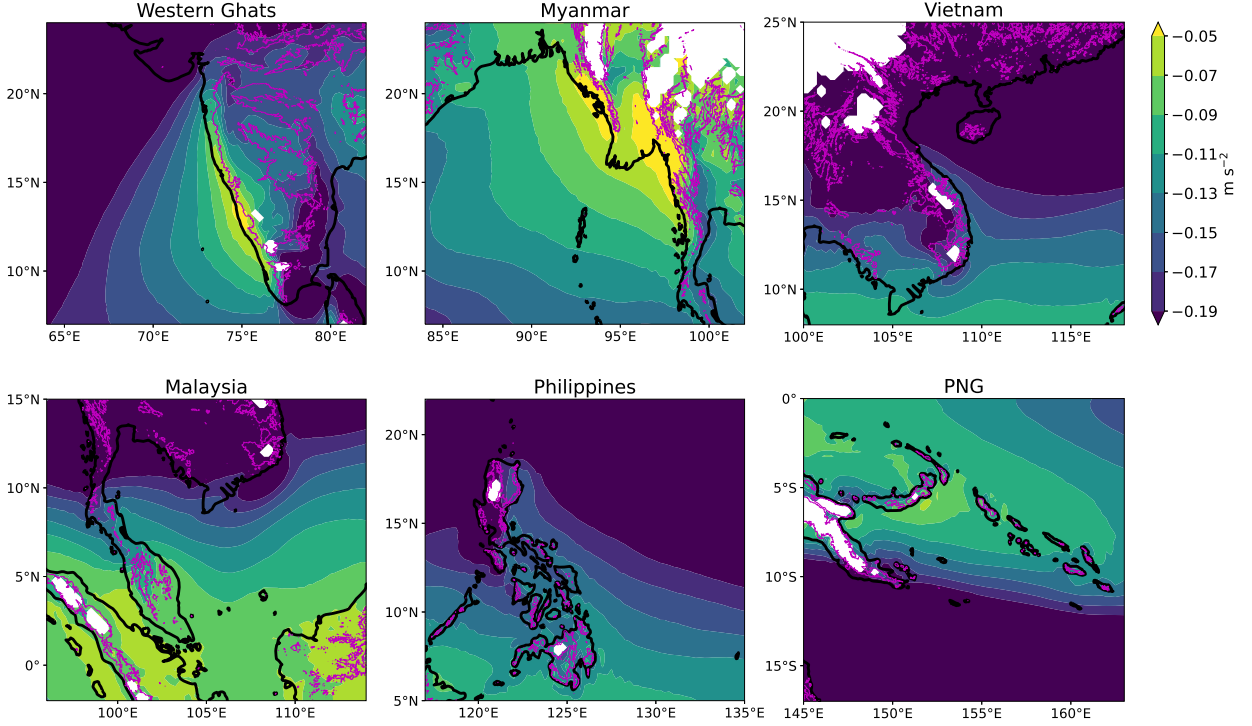
used to define the rain bands). Enhanced rainfall is associated with some amount of upslope flow in all regions, confirming the importance of orographic mechanical forcing in influencing precipitation variability there. Deviations from pure upslope flow (especially in Vietnam, Malaysia, the Philippines and PNG) are consistent with the wind patterns that accompany q_L variations (see Fig. 9), i.e. down-moisture gradient winds. This confirms the joint control of orographic lifting and large-scale moisture advection on orographic precipitation variability in the tropics.

Color shading in Fig. 10 shows precipitation regressed on this same upwind precipitation index. The existence of areas of weak positive association with the upwind rain index that are much wider than the orography indicate that orographic rainfall is partially controlled by large-scale, “background” precipitation variations. The stronger regression coefficients localized close to and preferentially upstream of the orography suggests the existence of an orographic mode of precipitation variability in each region. Patterns of positive association extend several hundred kilometers upstream of the regions used to define the rainfall index, as expected given the far-reaching influence of mechanical forcing upstream of a ridge (NB22).

5. Spatial distribution of buoyancy around orography

Strong spatial gradients are an ubiquitous characteristic of orographic rainfall. All regions in Fig. 3 exhibit a windward rainfall peak and a leeward rain shadow less than 200 km apart, with seasonal-mean precipitation rates varying from more than 15 mm day^{-1} to less than 5 mm day^{-1} on short distances. The buoyancy framework presented in section 4 naturally applies on short (hourly to daily) temporal scales, as buoyancy anomalies are consumed in a few hours (Ahmed et al. 2020). Here, we explore its potential to explain precipitation patterns on much longer time scales. Specifically, we explore whether seasonal-mean spatial features of orographic precipitation follow the spatial distribution of time-averaged buoyancy B_L .

The precipitation- B_L relationship was initially introduced as a nonlinear statistical relationship holding at short spatial and small temporal scales (Ahmed and Neelin 2018). It is statistical in the sense that a single value of B_L corresponds to a range of precipitation rates—the relationship appears when conditionally averaging precipitation. Taking time averages is thus favorable in that it eliminates the underlying stochasticity. However, averaging over a nonlinear relationship may yield a non-unique mapping between time-mean precipitation \bar{P} and time-mean buoyancy \bar{B}_L .



517 FIG. 11. Maps of seasonal-mean plume buoyancy B_L . The 500 m topography contour is shown in magenta.
 518 White shading represents undefined B_L values, wherever the surface pressure is lower than 900 hPa.

533 For example, it appears from Fig. 5 that the orographic rain band upstream of Myanmar has a
 534 narrower distribution of B_L than other regions. This suggests that $\overline{B_L}$ values in that region may
 535 be higher than in other places with comparable rain rates, e.g., upstream of the Western Ghats or
 536 PNG. Nonetheless, one might still expect a monotonic relationship between $\overline{B_L}$ and \overline{P} , perhaps
 537 with variations across regions.

538 We compute B_L from ERA5 temperature and moisture data at 0.25° and daily resolution, then
 539 average temporally over each region's雨季 (see Table 1) for 20 years. The resulting
 540 maps are shown in Fig. 11. We note that the boundary layer top is taken as the 900 hPa level,
 541 which ignores spatial variations in boundary layer depth. Including these variations (using ERA5
 542 estimates of boundary layer depth; not shown) does not affect the results presented here. Spatial
 543 features on these maps are broadly consistent with the maps of mean precipitation in Fig. 3. A
 544 distinct peak is visible upwind of each orographic barrier, with decreased B_L values in the lee: this
 545 confirms that mechanical forcing spatially distributes precipitation in a manner consistent with its
 546 effect on the temperature and moisture fields. This effect was already noted in Section 4 in the

maps of time-averaged T_L and q_L (Figs. 8 and 9, where upstream cold anomalies were present in all regions, and moist anomalies in several regions). B_L peaks are collocated with rainfall peaks (see Fig. 3) in all regions. One small exception is the easternmost B_L peak in Myanmar, which extends farther inland than the observed precipitation maximum. We note that the ERA5 precipitation distribution (not shown) follows the B_L pattern, with higher values than TRMM PR/GPM DPR inland. This may indicate that the reanalysis does not accurately represent the underlying B_L distribution there.

Except for the special case of Myanmar, rain shadows are consistent with the time-mean buoyancy distribution. Reduced values of B_L , mostly associated with a warmer and/or drier lower-troposphere, are visible downstream of the mountain ranges, consistent with the expected effect of gravity wave subsidence there. In the Western Ghats and in PNG, B_L does not drop as sharply as precipitation downstream of the rainfall maximum. Once again, ERA5 precipitation (not shown) partly reflects this fact, with overestimated rainfall values especially downstream of PNG. This could mean that ERA5 underestimates the warm and dry anomalies resulting from mechanically forced subsidence there (perhaps because the topography is under-resolved). Alternatively, the B_L framework may only partially account for the suppression of precipitation in rain shadows. Convection may be affected by higher-order variations in the vertical structures of temperature and moisture, or by neglected dynamical effects (e.g., mountain lees are regions of strong wind shear).

6. A linear model for seasonal-mean tropical orographic precipitation

Section 5 suggests that the spatial organization of tropical orographic rainfall is adequately captured by the time-mean plume buoyancy distribution. However, we have yet to quantify the effect of orography on this distribution. Here, we delve further into the physical drivers through which orography influences B_L and sets the strength and location of rainfall peaks and rain shadows. We use a simple theory that solves, for any topographic shape, the time-mean temperature and moisture anomalies carried by a stationary mountain wave (including convective feedback on the moisture anomalies) to estimate the time-mean precipitation distribution. The model describes mechanically forced rainfall in tropical regions, and neglects thermal forcing and Earth's rotation. We compare its predictions with observations and with two existing theories for mechanically forced orographic rainfall.

576 *a. Derivation*

577 The theory we present closely follows the one developed in NB22, but extends it to two horizontal
 578 dimensions. We give an outline of the derivation, and refer readers to that work for more details.
 579 A low-latitude domain with topography $h(x, y)$ has a constant background wind $\mathbf{u}_0 = (u_0, v_0)$ and
 580 Brunt-Väisälä frequency N . The flow is decomposed as the sum of a basic state, a “dry” mode (that
 581 carries temperature and moisture perturbations from a stationary mountain wave), and a “moist”
 582 mode (that consists of a convective response to these perturbations). The dry mode influences
 583 the moist mode by altering convective heating and moistening, that are parameterized as functions
 584 of lower-tropospheric temperature and moisture following the B_L framework, but the moist mode
 585 does not affect the dry mode. This simplifying assumption allows for analytical tractability, and
 586 was tested in NB22; idealized simulations showed that the moist mode does reduce the temperature
 587 perturbations carried by the dry mode, but that this effect is of second-order importance. In this
 588 section only, temperature and moisture are in energy units (compared to the previous sections, they
 589 are multiplied by c_p), for consistency with NB22.

590 Steady-state thermodynamic and moisture equations for the moist mode read:

$$\mathbf{u}_0 \cdot \nabla T_m + \omega_m \frac{ds_0}{dp} = Q_c - R, \quad (7a)$$

$$\mathbf{u}_0 \cdot \nabla q_m + \omega_m \frac{dq_0}{dp} = Q_q + E, \quad (7b)$$

591 where $s_0(p)$ and $q_0(p)$ are the background dry static energy profile and moisture profile (in energy
 592 units). Q_c and Q_q denote convective heating and moistening, while R and E are radiative cooling
 593 and surface evaporation rates. ω is the pressure velocity, and the subscript m is used for moist
 594 mode quantities (we will similarly use a subscript d for dry mode properties), so T_m and q_m are,
 595 respectively, the moist mode temperature and moisture perturbations.

596 We use the weak temperature gradient approximation for the moist mode, which implies that
 597 T_m is horizontally uniform. This allows us to set $T_m = 0$: one can add any horizontally uniform
 598 nonzero $T_m(p)$ to the reference profile $T_0(p)$, hence resulting in $T_m = 0$. Truncating the vertical
 599 velocity profile as $\omega_m(x, y, p) = \omega_1(x, y)\Omega(p)$, where Ω is a fixed vertical profile, and vertically

600 averaging over the depth of the troposphere yields

$$-\omega_1 M_s = \langle Q_c \rangle - \langle R \rangle, \quad (8a)$$

$$\mathbf{u}_0 \cdot \nabla \langle q_m \rangle + \omega_1 M_q = \langle Q_q \rangle + \langle E \rangle, \quad (8b)$$

601 where $M_s = -\langle \Omega \partial s_0 / \partial p \rangle$, $M_q = \langle \Omega \partial q_0 / \partial p \rangle$, and $\langle \cdot \rangle$ denotes a vertical average in pressure coordinates. $M = M_s - M_q$ is known as the gross moist stability, and M/M_s as the normalized gross moist stability (NGMS, Raymond et al. 2009).

604 Following Ahmed et al. (2020), the precipitation- B_L relationship is linearized (and boundary-layer θ_e is assumed constant), yielding

$$\langle Q_c \rangle = \frac{q'_L}{\tau_q} - \frac{T'_L}{\tau_T} = \frac{q_{dL} + q_{mL}}{\tau_q} - \frac{T_{dL}}{\tau_T}, \quad (9)$$

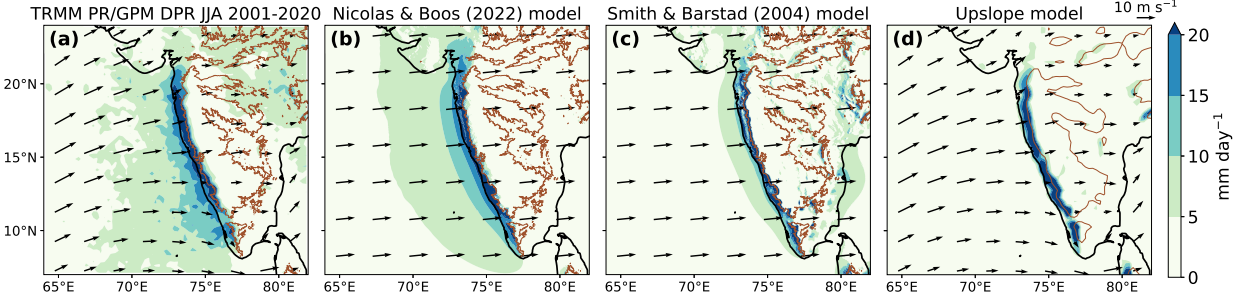
606 where q_{dL} and q_{mL} are lower-free-tropospheric moisture perturbations carried by the dry and
607 moist modes, T_{dL} is the dry mode temperature perturbation (recall $T_m = 0$), and the convective
608 time scales τ_T and τ_q are constants appearing from the linearization. For seasonal-mean rainfall,
609 these are taken as $\tau_T = 7.5$ hr and $\tau_q = 27.5$ hr, a factor 2.5 higher than their values when used to
610 represent precipitation at the hourly scale. Because the vertical structure of moisture perturbations
611 is horizontally uniform, q_{mL} and $\langle q_m \rangle$ are proportional to each other; we therefore define an
612 adjustment time scale for vertically averaged moisture, $\tilde{\tau}_q = 0.6\tau_q$ such that $q_{mL}/\tau_q = \langle q_m \rangle/\tilde{\tau}_q$.

613 We now use conservation of energy to relate convective heating, moistening, and precipitation
614 by

$$\langle Q_c \rangle = -\langle Q_q \rangle = \frac{\rho_w L_v g}{p_T} P, \quad (10)$$

615 where $p_T = 800$ hPa is the depth of the troposphere and $\rho_w = 1000 \text{ kg m}^{-3}$ is the density of water.
616 The first factor on the right-hand-side converts a precipitation rate (in m s^{-1} or mm day^{-1}) into a
617 convective heating rate (in $\text{J kg}^{-1} \text{s}^{-1}$). We henceforth define $\beta = p_T/(\rho_w L_v g)$. Using this definition
618 and combining (8a), (8b), (9), and (10), we derive an equation for P :

$$\mathbf{u}_0 \cdot \nabla P + \frac{\text{NGMS}}{\tilde{\tau}_q} (P - P_0) = \beta \mathbf{u}_0 \cdot \nabla \left(\frac{q_{dL}}{\tau_q} - \frac{T_{dL}}{\tau_T} \right), \quad (11)$$



619 FIG. 12. Maps of mean precipitation in the Western Ghats. (a) Observations (TRMM PR and GPM DPR), (b)
620 Nicolas and Boos (2022) theory, (c) Smith and Barstad (2004) theory, (d) upslope model ($\text{IVT} \cdot \nabla h / H_{\text{sat}}$).

621 where $P_0 = \beta \frac{M_s \langle E \rangle - M_q \langle R \rangle}{M}$ is a background rain rate. The right-hand-side of equation (11)
622 represents a forcing of convection by the dry mode. The second term on the left-hand-side
623 represents convective relaxation: precipitation forced by the cool and moist perturbations of
624 the dry mode dries the lower-free-troposphere, which in turn relaxes rainfall back towards the
625 background rate P_0 . The reverse process happens when precipitation is suppressed by warm
626 and dry perturbations. This process happens on a length scale $L_q = \tilde{\tau}_q |\mathbf{u}_0| / \text{NGMS}$. We note
627 that this framework is suitable for various vertical structures of convection, and that changes in
628 the vertical structure $\Omega(p)$ only affect the solutions through the NGMS. Remarkably, solutions
629 can be obtained with negative NGMS (which typically results from bottom-heavy vertical motion
630 profiles, e.g., Back and Bretherton 2006). In these cases, convection amplifies (rather than damps)
631 the precipitation perturbation forced by the dry mode.

632 Solving for T_{dL} and q_{dL} using mountain wave theory allows us to map a given topographic shape
633 to the associated precipitation distribution using a Fourier transform. In the dry mode, moisture is
634 conserved and there are no diabatic processes. Hence, horizontal advection terms are balanced by
635 vertical advection:

$$\mathbf{u}_0 \cdot \nabla \left(\frac{q_{dL}}{\tau_q} - \frac{T_{dL}}{\tau_T} \right) = w_{dL} \left(\frac{1}{\tau_T} \frac{ds_0}{dz} - \frac{1}{\tau_q} \frac{dq_0}{dz} \right), \quad (12)$$

636 where w_{dL} is the vertical velocity of the dry mode (we use height coordinates in the spirit of linear
 637 mountain wave theory). We define

$$\chi = \beta \left(\frac{1}{\tau_T} \frac{ds_0}{dz} - \frac{1}{\tau_q} \frac{dq_0}{dz} \right) \quad (13)$$

638 and substitute (12) into (11), which becomes (defining $P' = P - P_0$)

$$\mathbf{u}_0 \cdot \nabla P' + \frac{NGMS}{\tilde{\tau}_q} P' = \chi w_{dL}. \quad (14)$$

639 Here, w_{dL} is given by linear mountain wave theory, in two horizontal dimensions under the
 640 Boussinesq approximation, by (Smith 1979):

$$\hat{w}_d(k_x, k_y, z) = i\sigma \hat{h}(k_x, k_y) e^{im(k_x, k_y)z} \quad (15)$$

641 where k_x and k_y are the horizontal wavenumbers, hats denote Fourier transforms, $\sigma = k_x u_0 + k_y v_0$,
 642 and z is the vertical coordinate. Defining $K^2 = k_x^2 + k_y^2$, the vertical wavenumber $m(k_x, k_y)$ is

$$m = \begin{cases} \operatorname{sgn}(\sigma) \sqrt{K^2 \left(\frac{N^2}{\sigma^2} - 1 \right)} & \text{if } \sigma^2 < N^2 \\ i \sqrt{K^2 \left(1 - \frac{N^2}{\sigma^2} \right)} & \text{if } \sigma^2 > N^2 \end{cases}. \quad (16)$$

643 Fourier-transforming (14) and using (15) gives a closed expression for the Fourier-transformed
 644 precipitation anomaly \hat{P}' :

$$\hat{P}'(k_x, k_y) = \frac{i\sigma\chi}{i\sigma + \frac{NGMS}{\tilde{\tau}_q}} \hat{h}(k_x, k_y) \left[e^{im(k_x, k_y)z} \right]_L. \quad (17)$$

645 The main controlling parameters are topography $h(x)$, background wind u_0 , stratification N and
 646 a background moisture lapse rate. We note that in this model, the lower troposphere is defined
 647 between 1 km and 3 km above sea level. With this choice, mountain waves that have small
 648 vertical wavelengths may have positive temperature anomalies and negative moisture anomalies in
 649 the lower troposphere upstream of topography, and the model predicts small or negative rainfall
 650 enhancement in these cases. For $N \approx 0.01 \text{ s}^{-1}$, this happens when $U < 8 \text{ m s}^{-1}$; the model is not

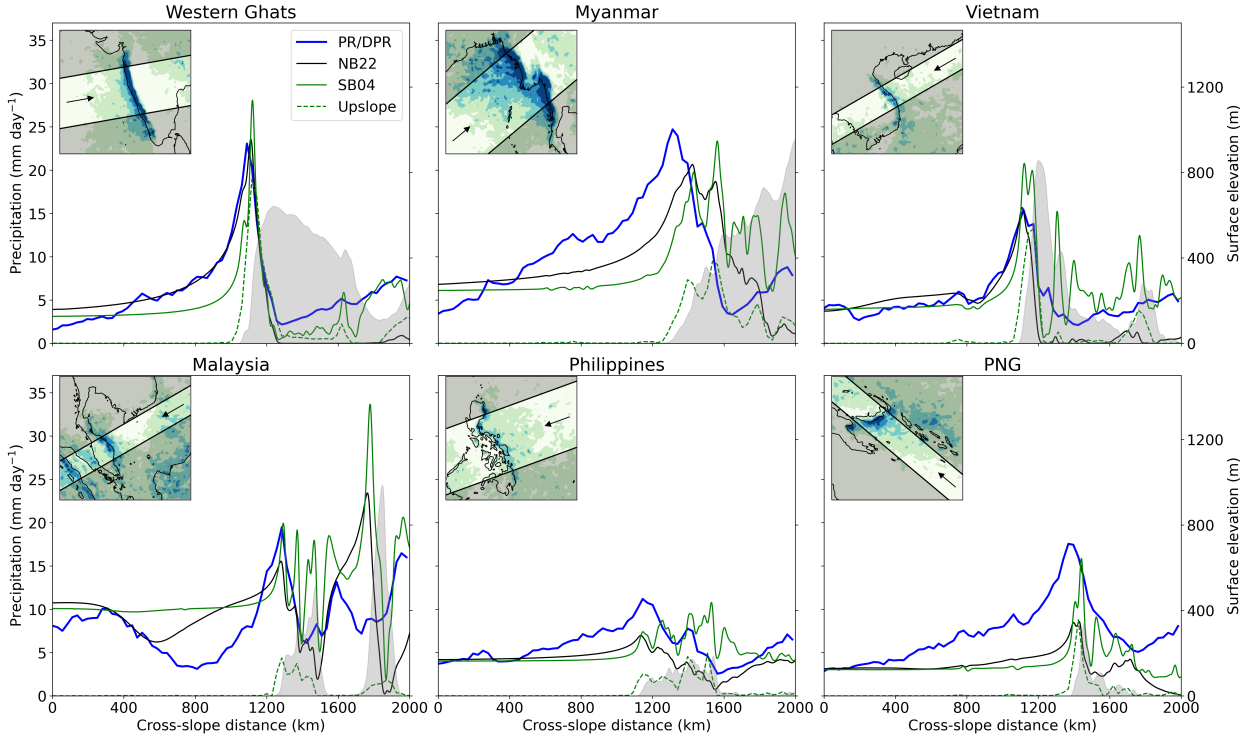
651 recommended for use below this wind speed without some attention to redefining the vertical span
652 of the lower troposphere, as well as taking thermal forcing into account. We now apply this model
653 to the real-world tropics.

654 *b. Comparing observed and modeled rainfall distributions*

651 The ingredients comprising the above theory (weak temperature gradient approximation,
652 quasiequilibrium precipitation closure) make it especially suited to tropical regions. SB04 de-
653 veloped a model of mechanically forced orographic rainfall for convectively stable flows that has
654 been used to represent midlatitude orographic precipitation. While SB04 did not intend their model
655 for use in tropical regions, it is arguably the most widely used theoretical model of orographic
656 precipitation, and as such provides a point of comparison with the present theory. Their model
657 assumes that condensation results from ascent in a saturated atmosphere (see (1)). Unlike the
658 upslope model, however, vertical motion is computed using linear mountain wave theory, and
659 the effects of finite hydrometeor growth times and downwind advection are parameterized. The
660 fundamental difference between the models of SB04 and NB22 is the mechanism linking mountain
661 waves to precipitation: in the former, rain is associated with the ascent rate w , while in the latter,
662 it is associated with vertical displacement of the lower-free-troposphere from a background state.
663 This results in shorter length scales for the upstream enhancement of rainfall and rain shadows
664 in SB04’s model. This can be understood qualitatively with the idealized topographic profile
665 used in the Appendix, which decays as $h(x) \propto x^{-2}$ upstream of the mountain; while the vertical
666 displacement should scale approximately like $h(x)$, the vertical motion will scale as dh/dx and
667 thus have a faster decay rate of x^{-3} .

668 We compare observed and modeled seasonal-mean rainfall maps⁴ in the Western Ghats in Fig.
669 12. Both the SB04 and NB22 models use a uniform static stability; we choose $N = 0.01 \text{ s}^{-1}$, which
670 corresponds to a lapse rate of 6.5 K km^{-1} , close to the free-tropospheric lapse rate in the Ghats.
671 Because tropical lapse rates are steeper than moist adiabats, we do not use SB04’s “moist static
672 stability” (which is negative in all regions) to calculate stationary mountain waves in the SB04
673 model. SB04 further require a moist adiabatic lapse rate, taken as $\Gamma_m = 4.3 \text{ K km}^{-1}$ (corresponding
674 to a lower-tropospheric average for a surface temperature of 300 K), and hydrometeor growth and

⁴For both models, the domain shown in Fig. 12 is padded to a square domain of side length 7500 km, with topography smoothed down to zero elevation 100 km outside of the main domain.



655 FIG. 13. Cross-sections of observed and modeled precipitation in all regions, along the direction of the
 656 seasonal-mean wind. The insets show the orientation and width of the areas used to define cross sections (the
 657 background shows mean observed precipitation from TRMM PR and GPM DPR, as in Fig. 3). The gray shadings
 658 represent topography. The dark blue lines are observed mean precipitation during each region's rainiest season.
 659 Other lines show precipitation from the Nicolas and Boos (2022) theory (black), the Smith and Barstad (2004)
 660 theory (solid green), and the upslope model (dashed green).

685 fallout times, both taken as 1000 s (as suggested in SB04). To account for non-precipitating times,
 686 the SB04 perturbation precipitation rates are divided by the factor 2.5, chosen in NB22 to fit peak
 687 rain rates from SB04 to convection-permitting simulations. For the NB22 model, we choose a
 688 lower-tropospheric moisture lapse rate of -8 K km^{-1} and NGMS = 0.2, representative of all the
 689 regions studied herein. Finally, the background wind and precipitation rate are given in Table 4,
 690 chosen to match upstream values from ERA5 and TRMM PR/GPM DPR. Both theories (Fig. 12,
 691 panels b and c) produce an upstream precipitation peak that is commensurate with observations
 692 (around 20 mm day⁻¹). As explained above, precipitation enhancement happens much closer to
 693 the ridge in the SB04 model, which fails to account for high precipitation rates over the Arabian
 694 sea upstream of the Western Ghats. It also predicts a second rainfall peak downstream, by the

695 eastern coast of India, associated with vertical motion predicted by linear mountain wave theory
696 there. This is unlike the NB22 model which features an extensive rain shadow. Although central
697 and northeastern India do receive precipitation during summer (panel a), this is commonly thought
698 to arise from the dynamics of synoptic-scale disturbances such as monsoon depressions (Sikka
699 1977) rather than mountain wave ascent downstream of the Indian topography.

700 For reference, Fig. 12d shows precipitation from the upslope model (eq. 2). We convert the
701 condensation rate into a precipitation rate using an efficiency factor $\epsilon = 0.25$, chosen to match peak
702 precipitation rates in the Ghats. We use $0.25^\circ \times 0.25^\circ$ topography, as higher resolutions lead to
703 unrealistic small-scale features in this model. Because it only predicts precipitation above mountain
704 slopes, it does not account for any upstream rainfall enhancement. By design, this model predicts
705 peak rainfall to occur on the steepest upstream slopes, and does capture a large part of the observed
706 peak directly above the windward Ghats.

707 We extend this analysis to all regions, and show cross-sectional averages of the observed and
708 modeled mean precipitation rates in Fig. 13. The insets show the direction and width of the cross
709 sections, which were chosen normal to topography and following the prevailing wind direction.
710 Background wind speeds and precipitation rates are listed in Table 4. With the fixed precipitation
711 efficiency $\epsilon = 0.25$ that produced a match to the peak precipitation magnitude in the Western
712 Ghats, the upslope model underestimates peak precipitation rates in nearly all other regions. Thus,
713 in addition to missing the upstream enhancement of precipitation, this model requires region-
714 specific tuning to yield accurate peak rainfall rates. The SB04 and NB22 models produce similar
715 peak rain rates in all regions, differing primarily in the upstream extent of the orographic rainfall
716 enhancement and in the leeside precipitation rates. The NB22 model accurately predicts the rainfall
717 enhancement upstream of certain regions (especially the Western Ghats and Vietnam), while the
718 SB04 model predicts rainfall to pick up much closer to the topography, at odds with observations.
719 The description of orographic rainfall as the result of forced temperature and moisture perturbations
720 in a lower-tropospheric quasiequilibrium state is thus consistent with observations there. In other
721 regions (most notably the Philippines and PNG), both models greatly underestimate precipitation
722 rates compared to observations. In the NB22 model, this failure results from an underestimation
723 of the moisture anomaly q'_L (not shown). We speculate that positive q_L perturbations are not only
724 the result of orographic lifting in these regions, and that climatological mean large-scale ascent,

TABLE 4. Parameters used in the precipitation models of Smith and Barstad (2004) and Nicolas and Boos (2022)

Region name	u_0 (m s $^{-1}$)	v_0 (m s $^{-1}$)	P_0 (mm day $^{-1}$)
Western Ghats	10	1	3
Myanmar	8	8	6
Vietnam	-7	-5	4
Malaysia	-7	-5	10
Philippines	-8.5	-3	4
PNG	-7.5	5.5	3

725 forced by non-orographic factors, plays a key role in producing the observed rainfall patterns. The
 726 fact that PNG is located within the SPCZ is consistent with this hypothesis.

727 Differences between observed and modeled precipitation rates are also apparent downstream
 728 of the mountain ranges. The NB22 model seems to strongly overestimate the drying effect of
 729 orography there. The main reason for this flaw is that the model assumes a time-independent
 730 background wind, which leads the lee of mountains to be persistently warm and dry. In reality,
 731 some days exhibit reversed flow or have a stronger along-slope component, creating more favorable
 732 conditions for convection in the lee. Additionally, synoptic disturbances (such as monsoon de-
 733 pressions downstream of the Indian subcontinent) may occasionally propagate into these regions,
 734 contributing to small positive seasonal-average precipitation there. As explained above in the case
 735 of the Western Ghats, the SB04 model predicts higher leeside precipitation rates, because linear
 736 mountain wave solutions produce ascent there. This leads to localized downstream precipitation
 737 peaks that are not seen in observations.

7. Discussion and conclusions

738 Here we investigated the spatial and temporal distribution of mechanically forced orographic
 739 rainfall in six tropical regions. We showed that a buoyancy proxy, evaluated from reanalysis data,
 740 captures many aspects of both daily variations and the seasonal-mean spatial distribution of rainfall
 741 in all regions. In this framework, the interaction of orography with the background wind creates
 742 temperature and moisture anomalies in the lower troposphere, affecting the buoyancy of convective
 743 plumes and thereby controlling precipitation.

745 This work confirms the important role of lower-free-tropospheric moisture (q_L) in controlling
 746 temporal variations in orographic convection. In the absence of background horizontal moisture

747 gradients, q_L variations would be fully controlled by orographic uplift, hence primarily by the
748 cross-slope wind speed. The presence of large-scale q_L gradients leads alternate directions of
749 wind anomalies to favor rainfall in some regions, namely down-moisture-gradient winds. These
750 results indicate that mechanical forcing only exerts a partial control on rainfall variations in the
751 regions studied. Together, these findings establish a new view of tropical orographic precipitation
752 being enhanced by moistening of the lower troposphere due to both upslope flow and large-scale
753 horizontal advection.

754 Despite the nonlinear relationship between plume buoyancy B_L and precipitation, time-averaged
755 B_L captures many spatial features of observed seasonal-mean precipitation maps. Discrepancies
756 appear in the rain shadows, where B_L (as estimated from a reanalysis) overestimates precipitation.
757 This points to a possible limitation of the present framework, in which convective dynamics are
758 assumed identical over oceans and in mountains, with mountains only affecting plume buoyancy.
759 Nevertheless, our goal here is to provide a first-order understanding of the mechanisms govern-
760 ing tropical orographic precipitation. We recognize that this approach neglects the influence of
761 some aspects of orographic dynamics, such as strong wind shears and gravity wave breaking, on
762 convection.

763 We present a linear theory that predicts the time-mean rainfall distribution for arbitrary 2D
764 topography and uniform wind. It quantifies the lower-tropospheric temperature and moisture per-
765 turbations caused by stationary mountain waves, and takes into account the feedback of convection
766 on the moisture distribution. The theory accurately predicts upstream rainfall in some regions,
767 especially the Western Ghats and Vietnam. In other regions (mainly the Philippines and PNG),
768 it yields weaker peak rainfall than observations. It is likely that mechanical forcing alone cannot
769 explain the strong rain bands observed there. The presence of climatological-mean ascent, due to
770 non-orographic factors (such as the SPCZ in PNG), plays a key role in setting the lower-tropospheric
771 moisture gradients, hence the rainfall patterns, in these regions.

772 The theoretical model presented herein only describes mechanically forced rainfall in tropical
773 regions. As such, it is expected to work with small nondimensional mountain heights and suf-
774 ficiently strong winds (we recommend its use for wind speeds of at least 8 m s^{-1}). The model
775 does not describe thermal forcing (expected to dominate in weak horizontal winds and/or large
776 nondimensional mountain heights), nor is it suitable for moist convectively stable ascent cases,

more common in midlatitude winter. Our use of the weak temperature gradient approximation for the moist mode, and neglect of the Coriolis parameter, may make it most appropriate for the tropics.

One other limitation of this study is that it does not investigate the vertical structure of convection, which past work has shown varies in tropical orographic regions (Kumar and Bhat 2017; Shige and Kummerow 2016). However, we have demonstrated that the buoyancy framework accurately characterizes precipitation in the six regions studied, irrespective of the mean depth of convection. Furthermore, the theoretical model assumes a fixed but arbitrary vertical structure of upward motion, and is thus applicable to a wide range of tropical regions (perhaps with modification of the coefficients that depend on the vertical structure of ascent). However, the buoyancy framework might not apply in trade wind regions, which are characterized by very shallow convection beneath an inversion layer (for a study of orographic precipitation in the trades, see Kirshbaum and Smith 2009).

This work suggests that two ingredients are needed to accurately represent tropical orographic convection: free-tropospheric temperature and moisture anomalies generated by flow over terrain, and the dependence of convection on those thermodynamic perturbations. This implies that a coarse-resolution model with a good convective parameterization may perform well around orography, as long as the magnitude of lower-tropospheric vertical displacement over the terrain is captured. We hope that future work will investigate the representation of tropical orographic rainfall in climate models under this lens.

797 *Acknowledgments.* This material is based on work supported by the U.S. Department of Energy,
 798 Office of Science, Office of Biological and Environmental Research, Climate and Environmental
 799 Sciences Division, Regional and Global Model Analysis Program, under Award DE-SC0019367.
 800 It used resources of the National Energy Research Scientific Computing Center (NERSC), which
 801 is a DOE Office of Science User Facility.

802 *Data availability statement.* The code containing linear precipitation models, the code used in
 803 producing the figures, and the processed ERA5 and precipitation data are archived at Zenodo
 804 (Nicolas 2023).

APPENDIX

806 Lower-tropospheric temperature and moisture perturbations forced by an idealized ridge

807 We consider an infinite two-dimensional (x - z) domain whose surface height is

$$h(x) = h_m \frac{l_0^2}{x^2 + l_0^2}, \quad (\text{A1})$$

808 where l_0 is the mountain half-width and h_m is the maximum height. This topographic profile,
 809 commonly known as a Witch-of-Agnesi, has a convenient Fourier transform, which renders the
 810 treatment of mountain wave solutions analytically tractable. The background horizontal wind speed
 811 U and static stability N are supposed uniform. We now estimate mechanically forced temperature
 812 perturbations using linear mountain wave theory, which is approximately valid under the assumption
 813 of small nondimensional mountain height Nh_m/U . Queney (1948) gives an analytical solution for
 814 $\zeta(x, z)$, the vertical displacement at x of a streamline originating upstream at z :

$$\zeta(x, z) = h_m \frac{\cos(Nz/U)l_0^2 - \sin(Nz/U)l_0x}{x^2 + l_0^2}. \quad (\text{A2})$$

815 This expression is valid when $l_0N/U \gg 1$, which is largely satisfied with a half-width $l_0 \simeq 100$
 816 km, $U \simeq 10 \text{ m s}^{-1}$, and $N \simeq 0.01 \text{ s}^{-1}$. With uniform static stability, and in the absence of diabatic
 817 processes, a parcel lifted by ζ experiences a cooling of magnitude $\zeta ds_0/dz$. Thus, the lower-free-

818 tropospheric temperature perturbation is

$$T'_L(x) = -h_m \frac{ds_0}{dz} \frac{\alpha_c l_0^2 - \alpha_s l_0 x}{x^2 + l_0^2}, \quad (\text{A3})$$

819 where $\alpha_c = [\cos(Nz/U)]_L$, $\alpha_s = [\sin(Nz/U)]_L$, and $[\cdot]_L$ denotes a lower-tropospheric average.
820 $s_0(z)$ is the background dry static energy profile profile (divided by c_p). Minimizing (A3) gives
821 the peak lower-tropospheric temperature perturbation:

$$T'_{L,\max} = -h_m \frac{ds_0}{dz} \left(\sqrt{\alpha_c^2 + \alpha_s^2} + \alpha_c \right), \quad (\text{A4})$$

822 Evaluating $\partial T'_{L,\max}/\partial U$ with a 1-km high mountain and $N = 0.01 \text{ s}^{-1}$ gives (5).

823 The peak moisture perturbation is given by the same expression as (A4), replacing ds_0/dz with
824 dq_0/dz (where $q_0(z)$ is a background moisture profile). Using a lower-free-tropospheric moisture
825 lapse rate representative of our regions (8 K km^{-1}), we obtain (6).

826 References

- 827 Ahmed, F., Á. F. Adames, and J. D. Neelin, 2020: Deep convective adjustment of temperature and
828 moisture. *Journal of the Atmospheric Sciences*, **77** (6), 2163 – 2186, <https://doi.org/10.1175/JAS-D-19-0227.1>.
- 830 Ahmed, F., and J. D. Neelin, 2018: Reverse engineering the tropical precipitation–buoyancy
831 relationship. *Journal of the Atmospheric Sciences*, **75** (5), 1587 – 1608, <https://doi.org/10.1175/JAS-D-17-0333.1>.
- 833 Amante, C., and B. Eakins, 2008: ETOPO1 1 arc-minute global relief model: Procedures, data
834 sources and analysis. *NOAA Technical Memorandum NESDIS NGDC-24. National Geophysical
835 Data Center, NOAA*, <https://doi.org/10.7289/V5C8276M>, accessed 10 Sep 2022.
- 836 Anber, U., S. Wang, and A. Sobel, 2014: Response of atmospheric convection to vertical wind shear:
837 Cloud-system-resolving simulations with parameterized large-scale circulation. Part I: Specified
838 radiative cooling. *Journal of the Atmospheric Sciences*, **71** (8), 2976 – 2993, <https://doi.org/10.1175/JAS-D-13-0320.1>.

- 840 Aoki, S., and S. Shige, 2024: Control of low-level wind on the diurnal cycle of tropical coastal
841 precipitation. *Journal of Climate*, **37** (1), 229 – 247, <https://doi.org/10.1175/JCLI-D-23-0180.1>.
- 842 Back, L. E., and C. S. Bretherton, 2006: Geographic variability in the export of moist static energy
843 and vertical motion profiles in the tropical Pacific. *Geophysical Research Letters*, **33** (17),
844 <https://doi.org/10.1029/2006GL026672>.
- 845 Bagtasa, G., 2020: Influence of Madden–Julian oscillation on the intraseasonal variability of
846 summer and winter monsoon rainfall in the Philippines. *Journal of Climate*, **33** (22), 9581 –
847 9594, <https://doi.org/10.1175/JCLI-D-20-0305.1>.
- 848 Biasutti, M., S. E. Yuter, C. D. Burleyson, and A. H. Sobel, 2012: Very high resolution rainfall pat-
849 terns measured by TRMM precipitation radar: seasonal and diurnal cycles. *Climate Dynamics*,
850 **39** (1), 239–258, <https://doi.org/10.1007/s00382-011-1146-6>.
- 851 Bretherton, C. S., M. E. Peters, and L. E. Back, 2004: Relationships between water vapor path and
852 precipitation over the tropical oceans. *Journal of Climate*, **17** (7), 1517 – 1528, <https://doi.org/>
853 [10.1175/1520-0442\(2004\)017<1517:RBWVPA>2.0.CO;2](https://doi.org/10.1175/1520-0442(2004)017<1517:RBWVPA>2.0.CO;2).
- 854 Chang, C.-P., Z. Wang, J. McBride, and C.-H. Liu, 2005: Annual cycle of Southeast
855 Asia—Maritime Continent rainfall and the asymmetric monsoon transition. *Journal of Climate*,
856 **18** (2), 287 – 301, <https://doi.org/10.1175/JCLI-3257.1>.
- 857 Chase, R. J., and H. A. Syed, 2022: dopplerchase/DRpy: First major release. Zenodo,
858 <https://doi.org/10.5281/zenodo.7259561>.
- 859 Chen, T.-C., J.-D. Tsay, M.-C. Yen, and J. Matsumoto, 2012: Interannual variation of the late
860 fall rainfall in central Vietnam. *Journal of Climate*, **25** (1), 392–413, <https://doi.org/10.1175/JCLI-D-11-0180.1>.
- 861
- 862 Chen, T.-C., J.-D. Tsay, M.-C. Yen, and J. Matsumoto, 2013: The winter rainfall of Malaysia.
863 *Journal of Climate*, **26** (3), 936 – 958, <https://doi.org/10.1175/JCLI-D-12-00174.1>.
- 864 Derbyshire, S. H., I. Beau, P. Bechtold, J.-Y. Grandpeix, J.-M. Piriou, J.-L. Redelsperger, and
865 P. M. M. Soares, 2004: Sensitivity of moist convection to environmental humidity. *Quarterly*

- 866 *Journal of the Royal Meteorological Society*, **130 (604)**, 3055–3079, <https://doi.org/10.1256/qj.03.130>.
- 868 Emanuel, K. A., J. David Neelin, and C. S. Bretherton, 1994: On large-scale circulations in
869 convecting atmospheres. *Quarterly Journal of the Royal Meteorological Society*, **120 (519)**,
870 1111–1143, <https://doi.org/10.1002/qj.49712051902>.
- 871 Espinoza, J. C., S. Chavez, J. Ronchail, C. Junquas, K. Takahashi, and W. Lavado, 2015: Rainfall
872 hotspots over the southern tropical Andes: Spatial distribution, rainfall intensity, and rela-
873 tions with large-scale atmospheric circulation. *Water Resources Research*, **51 (5)**, 3459–3475,
874 <https://doi.org/10.1002/2014WR016273>.
- 875 Grossman, R. G., and D. R. Durran, 1984: Interaction of low-level flow with the Western Ghat
876 mountains and offshore convection in the summer monsoon. *Monthly Weather Review*, **112**,
877 652–672, [https://doi.org/10.1175/1520-0493\(1984\)112<0652:IOLLFW>2.0.CO;2](https://doi.org/10.1175/1520-0493(1984)112<0652:IOLLFW>2.0.CO;2).
- 878 Hersbach, H., and Coauthors, 2018: ERA5 hourly data on pressure levels from 1959 to present.
879 Copernicus Climate Change Service (C3S) Climate Data Store (CDS), accessed: 2021-09-24,
880 <https://doi.org/10.24381/cds.bd0915c6>.
- 881 Hersbach, H., and Coauthors, 2020: The ERA5 global reanalysis. *Quarterly Journal of the Royal*
882 *Meteorological Society*, **146 (730)**, 1999–2049, <https://doi.org/10.1002/qj.3803>.
- 883 Houze, R. A., 2012: Orographic effects on precipitating clouds. *Reviews of Geophysics*, **50 (1)**,
884 <https://doi.org/10.1029/2011RG000365>.
- 885 Houze, R. A., K. L. Rasmussen, M. D. Zuluaga, and S. R. Brodzik, 2015: The variable nature
886 of convection in the tropics and subtropics: A legacy of 16 years of the Tropical Rainfall
887 Measuring Mission satellite. *Reviews of Geophysics*, **53 (3)**, 994–1021, <https://doi.org/10.1002/2015RG000488>.
- 888 Huffman, G. J., E. T. Stocker, D. T. Bolvin, E. J. Nelkin, and J. Tan, 2019: GPM IMERG Final
889 Precipitation L3 1 day 0.1 degree x 0.1 degree V06. Edited by Andrey Savtchenko, Greenbelt,
890 MD, Goddard Earth Sciences Data and Information Services Center (GES DISC), accessed:
891 2021-11-11, <https://doi.org/10.5067/GPM/IMERGDF/DAY/06>.

- 893 Hunt, K. M. R., A. G. Turner, T. H. M. Stein, J. K. Fletcher, and R. K. H. Schiemann, 2021: Modes
894 of coastal precipitation over southwest India and their relationship with intraseasonal variability.
895 *Quarterly Journal of the Royal Meteorological Society*, **147** (734), 181–201, <https://doi.org/10.1002/qj.3913>.
- 896
- 897 Iguchi, T., and R. Meneghini, 2021: GPM DPR Precipitation Profile 1 month 0.25 degree x 0.25
898 degree V07. Greenbelt, MD, Goddard Earth Sciences Data and Information Services Center
899 (GES DISC), accessed: 2023-09-10, <https://doi.org/10.5067/GPM/DPR/3A-MONTH/07>.
- 900
- 901 Johnston, B. R., W. J. Randel, and J. P. Sjoberg, 2021: Evaluation of tropospheric moisture
902 characteristics among COSMIC-2, ERA5 and MERRA-2 in the tropics and subtropics. *Remote
Sensing*, **13** (5), <https://doi.org/10.3390/rs13050880>.
- 903
- 904 Kirshbaum, D. J., B. Adler, N. Kalthoff, C. Barthlott, and S. Serafin, 2018: Moist orographic
905 convection: Physical mechanisms and links to surface-exchange processes. *Atmosphere*, **9** (3),
906 <https://doi.org/10.3390/atmos9030080>.
- 907
- 908 Kirshbaum, D. J., and R. B. Smith, 2008: Temperature and moist-stability effects on midlatitude
909 orographic precipitation. *Quarterly Journal of the Royal Meteorological Society*, **134** (634),
910 1183–1199, <https://doi.org/10.1002/qj.274>.
- 911
- 912 Kirshbaum, D. J., and R. B. Smith, 2009: Orographic precipitation in the tropics: Large-eddy
913 simulations and theory. *Journal of the Atmospheric Sciences*, **66** (9), 2559 – 2578, <https://doi.org/10.1175/2009JAS2990.1>.
- 914
- 915 Kumar, S., and G. S. Bhat, 2017: Vertical structure of orographic precipitating clouds observed
916 over south Asia during summer monsoon season. *Journal of Earth System Science*, **126** (8), 114,
917 <https://doi.org/10.1007/s12040-017-0897-9>.
- 918
- 919 Li, D., and Coauthors, 2022: High mountain Asia hydropower systems threatened by climate-
920 driven landscape instability. *Nature Geoscience*, **15** (7), 520–530, <https://doi.org/10.1038/s41561-022-00953-y>.
- 921
- 922 Lindzen, R. S., and S. Nigam, 1987: On the role of sea surface temperature gradients in forcing
923 low-level winds and convergence in the tropics. *Journal of Atmospheric Sciences*, **44** (17), 2418
924 – 2436, [https://doi.org/10.1175/1520-0469\(1987\)044<2418:OTROSS>2.0.CO;2](https://doi.org/10.1175/1520-0469(1987)044<2418:OTROSS>2.0.CO;2).
- 925

- 921 Lyon, B., H. Cristi, E. R. Verceles, F. D. Hilario, and R. Abastillas, 2006: Seasonal reversal of the
922 ENSO rainfall signal in the philippines. *Geophysical Research Letters*, **33** (24), <https://doi.org/10.1029/2006GL028182>.
- 924 National Geophysical Data Center, 2011: ETOPO1, Global 1 arc-minute ocean depth and land
925 elevation from the US National Geophysical Data Center (NGDC). Research Data Archive at the
926 National Center for Atmospheric Research, Computational and Information Systems Laboratory,
927 Boulder CO, accessed 10 Sep 2022, <https://doi.org/10.5065/D69Z92Z5>.
- 928 Nelson, T. C., J. Marquis, J. M. Peters, and K. Friedrich, 2022: Environmental controls on
929 simulated deep moist convection initiation occurring during RELAMPAGO-CACTI. *Journal of*
930 *the Atmospheric Sciences*, **79** (7), 1941 – 1964, <https://doi.org/10.1175/JAS-D-21-0226.1>.
- 931 Nicolas, Q., 2023: qnicolas/tropicalOrographicRegions: Revisions stage release. Zenodo,
932 <https://doi.org/10.5281/zenodo.10048884>.
- 933 Nicolas, Q., and W. R. Boos, 2022: A theory for the response of tropical moist convection to
934 mechanical orographic forcing. *Journal of the Atmospheric Sciences*, **79** (7), 1761 – 1779,
935 <https://doi.org/10.1175/JAS-D-21-0218.1>.
- 936 Nugent, A. D., R. B. Smith, and J. R. Minder, 2014: Wind speed control of tropical orographic
937 convection. *Journal of the Atmospheric Sciences*, **71** (7), 2695 – 2712, <https://doi.org/10.1175/JAS-D-13-0399.1>.
- 939 Ogura, Y., and M. Yoshizaki, 1988: Numerical study of orographic-convective precipitation over
940 the eastern Arabian sea and the Ghat mountains during the summer monsoon. *Journal of At-*
941 *mospheric Sciences*, **45** (15), 2097 – 2122, [https://doi.org/10.1175/1520-0469\(1988\)045<2097: NSOOCP>2.0.CO;2](https://doi.org/10.1175/1520-0469(1988)045<2097: NSOOCP>2.0.CO;2).
- 943 Oouchi, K., A. T. Noda, M. Satoh, B. Wang, S.-P. Xie, H. G. Takahashi, and T. Yasunari,
944 2009: Asian summer monsoon simulated by a global cloud-system-resolving model: Diurnal
945 to intra-seasonal variability. *Geophysical Research Letters*, **36** (11), <https://doi.org/10.1029/2009GL038271>.

- 947 Peters, J. M., H. Morrison, T. C. Nelson, J. N. Marquis, J. P. Mulholland, and C. J. Nowotarski,
948 2022a: The influence of shear on deep convection initiation. Part I: Theory. *Journal of the*
949 *Atmospheric Sciences*, **79** (6), 1669 – 1690, <https://doi.org/10.1175/JAS-D-21-0145.1>.
- 950 Peters, J. M., H. Morrison, T. C. Nelson, J. N. Marquis, J. P. Mulholland, and C. J. Nowotarski,
951 2022b: The influence of shear on deep convection initiation. Part II: Simulations. *Journal of the*
952 *Atmospheric Sciences*, **79** (6), 1691 – 1711, <https://doi.org/10.1175/JAS-D-21-0144.1>.
- 953 Pradhan, R. K., and Coauthors, 2022: Review of GPM IMERG performance: A global perspective.
954 *Remote Sensing of Environment*, **268**, 112 754, <https://doi.org/10.1016/j.rse.2021.112754>.
- 955 Queney, P., 1948: The problem of air flow over mountains: A summary of theoretical
956 studies. *Bulletin of the American Meteorological Society*, **29** (1), 16 – 26, <https://doi.org/10.1175/1520-0477-29.1.16>.
- 958 Ramesh, N., Q. Nicolas, and W. R. Boos, 2021: The globally coherent pattern of au-
959 tumn monsoon precipitation. *Journal of Climate*, **34** (14), 5687 – 5705, <https://doi.org/10.1175/JCLI-D-20-0740.1>.
- 961 Raymond, D., Ž. Fuchs, S. Gjorgjevska, and S. Sessions, 2015: Balanced dynamics and convection
962 in the tropical troposphere. *Journal of Advances in Modeling Earth Systems*, **7** (3), 1093–1116,
963 <https://doi.org/10.1002/2015MS000467>.
- 964 Raymond, D. J., S. L. Sessions, A. H. Sobel, and Ž. Fuchs, 2009: The mechanics of gross moist
965 stability. *Journal of Advances in Modeling Earth Systems*, **1** (3).
- 966 Revadekar, J., H. Varikoden, P. Murumkar, and S. Ahmed, 2018: Latitudinal variation in
967 summer monsoon rainfall over Western Ghat of India and its association with global sea
968 surface temperatures. *Science of The Total Environment*, **613-614**, 88–97, <https://doi.org/10.1016/j.scitotenv.2017.08.285>.
- 970 Robe, F. R., and K. A. Emanuel, 2001: The effect of vertical wind shear on radiative–convective
971 equilibrium states. *Journal of the Atmospheric Sciences*, **58** (11), 1427 – 1445, [https://doi.org/10.1175/1520-0469\(2001\)058<1427:TEOVWS>2.0.CO;2](https://doi.org/10.1175/1520-0469(2001)058<1427:TEOVWS>2.0.CO;2).

- 973 Robertson, A. W., V. Moron, J.-H. Qian, C.-P. Chang, F. Tangang, E. Aldrian, T. Y. Koh, and
974 J. Liew, 2011: The maritime continent monsoon. *The Global Monsoon System: Research and*
975 *Forecast*, 2nd ed., World Scientific, 85–98, https://doi.org/10.1142/9789814343411_0006.
- 976 Roe, G. H., 2005: Orographic precipitation. *Annual Review of Earth and Planetary Sciences*,
977 **33** (1), 645–671, <https://doi.org/10.1146/annurev.earth.33.092203.122541>.
- 978 Sawyer, J. S., 1956: The physical and dynamical problems of orographic rain. *Weather*, **11** (12),
979 375–381, <https://doi.org/10.1002/j.1477-8696.1956.tb00264.x>.
- 980 Seto, S., T. Iguchi, R. Meneghini, J. Awaka, T. Kubota, T. Masaki, and N. Takahashi, 2021: The
981 precipitation rate retrieval algorithms for the GPM dual-frequency precipitation radar. *Journal*
982 *of the Meteorological Society of Japan. Ser. II*, **99** (2), 205–237, <https://doi.org/10.2151/jmsj.2021-011>.
- 984 Shige, S., and C. D. Kummerow, 2016: Precipitation-top heights of heavy orographic rainfall
985 in the Asian monsoon region. *Journal of the Atmospheric Sciences*, **73** (8), 3009 – 3024,
986 <https://doi.org/10.1175/JAS-D-15-0271.1>.
- 987 Shige, S., Y. Nakano, and M. K. Yamamoto, 2017: Role of orography, diurnal cycle, and in-
988 traseasonal oscillation in summer monsoon rainfall over the Western Ghats and Myanmar coast.
989 *Journal of Climate*, **30** (23), 9365 – 9381, <https://doi.org/10.1175/JCLI-D-16-0858.1>.
- 990 Shrestha, D., R. Deshar, and K. Nakamura, 2015: Characteristics of summer precipitation around
991 the Western Ghats and the Myanmar west coast. *International Journal of Atmospheric Sciences*,
992 **2015**, 206 016, <https://doi.org/10.1155/2015/206016>.
- 993 Sijikumar, S., L. John, and K. Manjusha, 2013: Sensitivity study on the role of Western Ghats in
994 simulating the Asian summer monsoon characteristics. *Meteorology and Atmospheric Physics*,
995 **120** (1), 53–60, <https://doi.org/10.1007/s00703-013-0238-8>.
- 996 Sikka, D. R., 1977: Some aspects of the life history, structure and movement of monsoon depres-
997 sions. *Pure and Applied Geophysics*, **115** (5), 1501–1529, <https://doi.org/10.1007/BF00874421>.
- 998 Smith, I., A. Moise, K. Inape, B. Murphy, R. Colman, S. Power, and C. Chung, 2013: ENSO-related
999 rainfall changes over the New Guinea region. *Journal of Geophysical Research: Atmospheres*,
1000 **118** (19), 10,665–10,675, <https://doi.org/10.1002/jgrd.50818>.

- ¹⁰⁰¹ Smith, R. B., 1979: The influence of mountains on the atmosphere. *Advances in Geophysics*, **21**,
¹⁰⁰² 87–230, [https://doi.org/10.1016/S0065-2687\(08\)60262-9](https://doi.org/10.1016/S0065-2687(08)60262-9).
- ¹⁰⁰³ Smith, R. B., 1989: Hydrostatic airflow over mountains. *Advances in Geophysics*, **31**, 1–41.
- ¹⁰⁰⁴ Smith, R. B., 2019: 100 Years of Progress on Mountain Meteorology Research. *Meteorological Monographs*, Vol. 59, American Meteorological Society, 20, <https://doi.org/10.1175/AMSMONOGRAPHSD-18-0022.1>.
- ¹⁰⁰⁷ Smith, R. B., and I. Barstad, 2004: A linear theory of orographic precipitation. *Journal of the Atmospheric Sciences*, **61** (12), 1377 – 1391, [https://doi.org/10.1175/1520-0469\(2004\)061<1377:ALTOOP>2.0.CO;2](https://doi.org/10.1175/1520-0469(2004)061<1377:ALTOOP>2.0.CO;2).
- ¹⁰¹⁰ Smith, R. B., and Y.-L. Lin, 1983: Orographic rain on the Western Ghats. *Proceedings of the First Sino-American Workshop on Mountain Meteorology*, 71–94.
- ¹⁰¹² Sobel, A. H., C. D. Burleyson, and S. E. Yuter, 2011: Rain on small tropical islands. *Journal of Geophysical Research: Atmospheres*, **116** (D8), <https://doi.org/10.1029/2010JD014695>.
- ¹⁰¹⁴ Sobel, A. H., J. Nilsson, and L. M. Polvani, 2001: The weak temperature gradient approximation and balanced tropical moisture waves. *Journal of the Atmospheric Sciences*, **58** (23), 3650 – 3665, [https://doi.org/10.1175/1520-0469\(2001\)058<3650:TWTGAA>2.0.CO;2](https://doi.org/10.1175/1520-0469(2001)058<3650:TWTGAA>2.0.CO;2).
- ¹⁰¹⁷ Tawde, S. A., and C. Singh, 2015: Investigation of orographic features influencing spatial distribution of rainfall over the Western Ghats of India using satellite data. *International Journal of Climatology*, **35** (9), 2280–2293, <https://doi.org/10.1002/joc.4146>.
- ¹⁰²⁰ Tropical Rainfall Measuring Mission, 2021: GPM PR on TRMM Reflectivity, Precipitation Statistics, Histograms, at Surface and Fixed Heights, 1 month 5x5 and 0.25x0.25 degree V07. Greenbelt, MD, Goddard Earth Sciences Data and Information Services Center (GES DISC), accessed: 2023-09-10, <https://doi.org/10.5067/GPM/PR/TRMM/3A-MONTH/07>.
- ¹⁰²⁴ Van den Hende, C., B. Van Schaeybroeck, J. Nyssen, S. Van Vooren, M. Van Genderachter, and P. Termonia, 2021: Analysis of rain-shadows in the Ethiopian mountains using climatological model data. *Climate Dynamics*, **56** (5), 1663–1679, <https://doi.org/10.1007/s00382-020-05554-2>.

- 1028 Vivioli, D., M. Kummu, M. Meybeck, M. Kallio, and Y. Wada, 2020: Increasing dependence
1029 of lowland populations on mountain water resources. *Nature Sustainability*, **3** (11), 917–928,
1030 <https://doi.org/10.1038/s41893-020-0559-9>.
- 1031 Wang, S., and A. H. Sobel, 2017: Factors controlling rain on small tropical islands: Diurnal
1032 cycle, large-scale wind speed, and topography. *Journal of the Atmospheric Sciences*, **74** (11),
1033 3515–3532.
- 1034 Wilks, D. S., 2016: “The stippling shows statistically significant grid points”: How research results
1035 are routinely overstated and overinterpreted, and what to do about it. *Bulletin of the American
1036 Meteorological Society*, **97** (12), 2263 – 2273, <https://doi.org/10.1175/BAMS-D-15-00267.1>.
- 1037 Wu, C.-H., W.-R. Huang, and S.-Y. S. Wang, 2018: Role of Indochina peninsula topography in pre-
1038 cipitation seasonality over east Asia. *Atmosphere*, **9** (7), <https://doi.org/10.3390/atmos9070255>.
- 1039 Xie, S., T. Hume, C. Jakob, S. A. Klein, R. B. McCoy, and M. Zhang, 2010: Observed large-scale
1040 structures and diabatic heating and drying profiles during TWP-ICE. *Journal of Climate*, **23** (1),
1041 57 – 79, <https://doi.org/https://doi.org/10.1175/2009JCLI3071.1>.
- 1042 Xie, S.-P., H. Xu, N. H. Saji, Y. Wang, and W. T. Liu, 2006: Role of narrow mountains in large-
1043 scale organization of Asian monsoon convection. *Journal of Climate*, **19** (14), 3420 – 3429,
1044 <https://doi.org/10.1175/JCLI3777.1>.
- 1045 Xu, K.-M., and K. A. Emanuel, 1989: Is the tropical atmosphere conditionally unstable? *Monthly
1046 Weather Review*, **117** (7), 1471 – 1479, [https://doi.org/10.1175/1520-0493\(1989\)117<1471:ITTACU>2.0.CO;2](https://doi.org/10.1175/1520-0493(1989)117<1471:ITTACU>2.0.CO;2).
- 1048 Yen, M.-C., T.-C. Chen, H.-L. Hu, R.-Y. Tzeng, D. T. Dinh, T. T. T. Nguyen, and C. J. Wong,
1049 2011: Interannual variation of the fall rainfall in central Vietnam. *Journal of the Meteorological
1050 Society of Japan. Ser. II*, **89A**, 259–270, <https://doi.org/10.2151/jmsj.2011-A16>.
- 1051 Zhang, G., and R. B. Smith, 2018: Numerical study of physical processes controlling sum-
1052 mer precipitation over the Western Ghats region. *Journal of Climate*, **31** (8), 3099 – 3115,
1053 <https://doi.org/10.1175/JCLI-D-17-0002.1>.